

Aerosol optical properties in the Arctic: The role of aerosol chemistry and dust composition in a closure experiment between Lidar and tethered balloon vertical profiles



L. Ferrero ^{a,*}, C. Ritter ^b, D. Cappelletti ^{c,d}, B. Moroni ^c, G. Močnik ^e, M. Mazzola ^d, A. Lupi ^d, S. Becagli ^{d,f}, R. Traversi ^{d,f}, M. Cataldi ^a, R. Neuber ^b, V. Vitale ^d, E. Bolzacchini ^a

^a GEMMA and POLARIS Research Centers, Department of Earth and Environmental Sciences, University of Milano-Bicocca, Piazza della Scienza 1, 20126 Milan, Italy

^b Alfred-Wegener Institut für Polar- und Meeresforschung (AWI), Forschungsstelle Potsdam, Telegrafenbergh 43A, 14473 Potsdam, Germany

^c Department of Chemistry, Biology and Biotechnology, University of Perugia, Via Elce di Sotto 8, 06123 Perugia, Italy

^d National Research Council, Institute of Atmospheric Sciences and Climate, (CNR-ISAC), Via P. Gobetti 101, 40129 Bologna, Italy

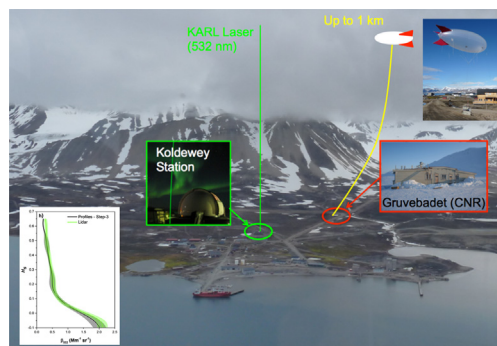
^e Department of Condensed Matter Physics, Jozef Stefan Institute, Jamova 39, SI-1000 Ljubljana, Slovenia

^f Department of Chemistry, University of Florence, Via della Lastruccia 3, 50019 Sesto Fiorentino, Florence, Italy

HIGHLIGHTS

- Lidar and tethered balloon-based aerosol vertical profiles were measured concurrently in the Arctic.
- Aerosol chemistry and size distribution were measured during the campaign.
- SEM-EDS analyses of dust transport were included in the study.
- The refractive index was determined from full chemical composition.
- Closure between lidar and balloon-based optical profiles was performed with Mie calculations.

GRAPHICAL ABSTRACT



ARTICLE INFO

Article history:

Received 24 February 2019

Received in revised form 21 May 2019

Accepted 26 May 2019

Available online 1 June 2019

Editor: Pingqiang Fu

Keywords:

Aerosol
Svalbard
Optical properties
Back scattering
Chemical composition

ABSTRACT

A closure experiment was conducted over Svalbard by comparing Lidar measurements and optical aerosol properties calculated from aerosol vertical profiles measured using a tethered balloon. Arctic Haze was present together with Icelandic dust. Chemical analysis of filter samples, aerosol size distribution and a full set of meteorological parameters were determined at ground. Moreover, scanning electron microscopy coupled with energy-dispersive X-ray (SEM-EDS) data were at disposal showing the presence of several mineralogical phases (i.e., sheet silicates, gypsum, quartz, rutile, hematite).

The closure experiment was set up by calculating the backscattering coefficients from tethered balloon data and comparing them with the corresponding lidar profiles. This was performed in three subsequent steps aimed at determining the importance of a complete aerosol speciation: (i) a simple, columnar refractive index was obtained by the closest Aerosol Robotic Network (AERONET) station, (ii) the role of water-soluble components, elemental carbon and organic matter (EC/OM) was addressed, (iii) the dust composition was included.

When considering the AERONET data, or only the ionic water-soluble components and the EC/OM fraction, results showed an underestimation of the backscattering lidar signal up to 76, 53 and 45% (355, 532 and

* Corresponding author.

E-mail address: luca.ferrero@unimib.it (L. Ferrero).

Icelandic dust
Lidar

1064 nm). Instead, when the dust contribution was included, the underestimation disappeared and the vertically-averaged, backscattering coefficients (1.45 ± 0.30 , 0.69 ± 0.15 and $0.34 \pm 0.08 \text{ Mm}^{-1} \text{ sr}^{-1}$, at 355, 532 and 1064 nm) were found in keeping with the lidar ones (1.60 ± 0.22 , 0.75 ± 0.16 and $0.31 \pm 0.08 \text{ Mm}^{-1} \text{ sr}^{-1}$). Final results were characterized by low RMSE (0.36, 0.08 and $0.04 \text{ Mm}^{-1} \text{ sr}^{-1}$) and a high linear correlation (R^2 of 0.992, 0.992 and 0.994) with slopes close to one (1.368, 0.931 and 0.977, respectively). This work highlighted the importance of all the aerosol components and of the synergy between single particle and bulk chemical analysis for the optical property characterization in the Arctic.

© 2019 Elsevier B.V. All rights reserved.

1. Introduction

In the Arctic, the temperature increase due to climate change is almost twice faster than globally, a phenomenon called Arctic amplification (Bindi et al., 2018; Sand et al., 2015; Serreze and Barry, 2011; Shindell and Faluvegi, 2009). The role of atmospheric aerosols is significant to the Arctic warming and is related the worldwide changes in the aerosol chemical composition (e.g. sulfates reduction and increased black carbon (BC) concentrations and its deposition on snow/ice) (Navarro et al., 2016; Flanner, 2013; Serreze and Barry, 2011; Shindell and Faluvegi, 2009; Hansen and Nazarenko, 2004). Shindell and Faluvegi (2009) estimated that the variation in the aerosol properties globally contributed with $1.09 \pm 0.81 \text{ }^\circ\text{C}$ to the Arctic surface temperature increase of $1.48 \pm 0.28 \text{ }^\circ\text{C}$ (for the period 1976–2007). This phenomenology, was recently confirmed by Navarro et al. (2016).

In this respect, the aerosol chemistry influences its direct, indirect and semi-direct effects (IPCC, 2013; Ramanathan and Feng, 2009; Koren et al., 2008; Koren et al., 2004; Kaufman et al., 2002).

Moreover, several aerosol-related processes and feedbacks can enhance the Arctic amplification: the sea ice changes (Screen and Simmonds 2010a and 2010b), the variation of heat transported by the atmosphere (and the ocean) (Yang et al., 2010), the cloud cover and water vapour changes (Francis and Hunter, 2006).

In the Arctic, the aerosol properties experience a pronounced seasonal variation, due to changes in the dominating sources and long-range transport regimes (Quinn et al., 2008): the spring period is dominated by the presence of the Arctic Haze (mainly accumulation mode aerosol enriched in black carbon, BC) and it is followed by a summer period in which nucleation takes place originating small Aitken particles (Dall' Osto et al., 2017; Giardi et al., 2016; Udisti et al., 2016, 2013; Tunved et al., 2013; Eleftheriadis et al., 2009). In addition to this, both during spring and summer dust transport can happen. Particularly, high latitude dust source (e.g. Icelandic dust) can affect the aerosol burden injecting into the atmosphere $\sim 4\text{--}40 \text{ Tg year}^{-1}$ of material, of which, $\sim 7\%$ can reach the Arctic (Moroni et al., 2018; Groot Zwaafink et al., 2016, 2017).

All the aforementioned seasonal aerosol properties become important when observed in the vertical direction. As a matter of fact, the aerosol effects (warming or cooling) and the related feedbacks (i.e. direct effect, snow/ice-albedo, clouds) are strictly determined by the vertical variation of their optical, chemical, dimensional and morphological properties (Flanner, 2013; Sand et al., 2013; Ban-Weiss et al., 2011; Shindell and Faluvegi, 2009; Ferrero et al., 2016).

In this respect, it has been recently demonstrated that the final vertical aerosol synergy between the seasonal behaviour of aerosol and the local meteorology results in a seasonal phenomenology of vertical aerosol properties in which different sources may shape the aerosol at different altitudes (Ferrero et al., 2016; Brock et al., 2011; Jacob et al., 2010 and reference therein). For example, Brock et al. (2011) (ARCPAC campaign) grouped the spring-time Arctic aerosol in background aerosol (sulfate-rich, relatively diffuse), depleted aerosol over sea-ice (within the surface inversion layer), organic-rich aerosol (biomass above the top of the inversion layer) and by fossil fuel dominated layers. Ferrero et al. (2016), instead, grouped the spring-time Arctic aerosol according to their shape describing: 1) homogeneous profiles (HO: constant

properties with altitude; 15% of occurrence) related to Arctic background conditions; 2) positive and negative gradient profiles (PG and NG: increase and decrease of concentration with altitude influenced by long-range transport; 17% and 48% of occurrence) related to Arctic Haze advection and injection into the planetary boundary layer (PBL); 3) decoupled negative gradient profiles (DNG: negative gradients located at different altitude in function of size; 20% of occurrence) related to a secondary aerosol formation close the ground, typically occurring in late spring.

The importance of these classes is related to their feedback on climate (Samset et al., 2013). An increase of aerosols with altitude can influence the cloud cover (inducing mainly a positive forcing) while aerosol and BC/dust layers located immediately above snow and ice may induce a positive forcing, the opposite of the effect they can induce at high altitude (Dall' Osto et al., 2017; Flanner, 2013; Sand et al., 2013; Vavrus et al., 2009; Intrieri et al., 2002).

Thus, there is a clear need to perform continuous vertical profile measurements in the Arctic to improve the description of a seasonally resolved aerosol vertical behaviour. However, aircraft-, helicopters-, UAV- or balloon-based vertical profile measurements can be conducted mainly during intensive observational periods (Ferrero et al., 2016; Brock et al., 2011; Jacob et al., 2010; Kupiszewski et al., 2013; Bates et al., 2013; Spackman et al., 2010; Schwarz et al., 2010; Koch et al., 2009) making them scarce if compared with the number of available data collected at ground level (Samset et al., 2013; Koch et al., 2009).

Conversely, remote sensing techniques, such as lidar measurements (Chaikovsky et al., 2016) can overcome this limitation and also become complementary to in-situ measurements (i.e., aircraft, balloon); in this respect, Markowicz et al. (2017) recently demonstrated the capability to determine the vertical profile of single scattering albedo (SSA) coupling lidar extinction profiles with tethered balloon-based absorption coefficient profiles. The SSA uncertainty reported in their work ranged between ± 0.01 to ± 0.04 . Thus, closure experiments becomes fundamental to reduce these uncertainties as well as, when successfully carried out, to take advantage of and use in synergy the long-term data series of aerosol properties collected with different techniques characterized by different spatial and temporal resolution (Tesche et al., 2014). In this respect, the growing number of vertical profiles directly measured in the Arctic in recent years (i.e. ARTCAS, ARCPAC, ASTAR, ASCOS and ARCTICA2009 campaign) (Ferrero et al., 2016; Mazzola et al., 2016; Moroni et al., 2015; Kupiszewski et al., 2013; Brock et al., 2011; Jacob et al., 2010; Engvall et al., 2008) and the long-term data series of lidar, radiometric and meteorological data (Maturilli and Kayser, 2016; Tunved et al., 2013; Di Liberto et al., 2012; Vihma et al., 2011; Hoffmann et al., 2009; Hoffmann, 2012) represent a unique opportunity.

However, despite this massive amount of data, closure experiments are still sparse. Hoffmann et al. (2012) compared lidar-derived size distributions at two different altitudes to in-situ measurements by DMPS at the close-by Zeppelin station at 474 m ASL. A fair agreement has been found for a long-lasting event of Arctic Haze in 2009. However, closure studies are by no means straightforward and may critically depend on the time and humidity dependent aerosol properties. For example, Tesche et al. (2014) reported a significant over-estimation of extinction from remote sensing data (lidar of the Calipso satellite) compared to in-

situ measurements which could be minimized if the most similar back-trajectories had been compared instead of the closest matching profiles. Thus, there is a clear need to perform closure experiments about vertical aerosol profiles in the Arctic especially during different types of vertical behaviour in function of the aerosol composition.

This paper tries to fill this gap reporting a closure experiment between tethered balloon-based and vertical lidar profiles measured over Ny-Ålesund (Svalbard Islands) collected in the framework of the PRIN2009 “ARCTICA” project and the KOL09/RIS2399 “derivation of aerosol properties by lidar” project. Notably, this work takes advantage of the aerosol phenomenology along vertical profiles described over Ny-Ålesund (Svalbard Islands) during a two years long extensive field campaign (2011–2012; 200 vertical profiles). The vertical aerosol behaviour was used as a primary criterion to perform a targeted closure experiment in conditions representative for the Arctic. Moreover, the closure experiment was set up in three subsequent steps aiming at highlighting the need for a complete aerosol chemical determination to preform a perfect closure.

2. Methodology

2.1. Measurement location and date

The present closure experiment considers tethered balloon and vertical lidar profiles carried out over Ny-Ålesund (Svalbard) during spring 2011. The measurement site faces northwards at sea in the Kongsfjorden (north-west southeasterly direction) while a small chain of 500–800 m high mountains is located to the South. Tethered balloon profiles were measured from the Italian CNR Gruvebadet sampling site ($78^{\circ}55'03''\text{N}$ $11^{\circ}53'40''\text{E}$; Fig. 1) (Cappelletti et al., 2016) which is located ~1 km southern Ny-Ålesund and ~1300 m far from the mountain base ensuring a negligible impact form local (Ny-Ålesund) emissions (a restricted, clean area was established around the site).

Lidar profiles were carried out from the German research base ($78^{\circ}55'24''\text{N}$ $11^{\circ}55'15''\text{E}$) ~600 m northward from Gruvebadet and ~600 m far from the fjord (Fig. 1).

Among the whole dataset, reported and discussed in Ferrero et al. (2016), this work focuses on a subset of lidar and tethered balloon measurements that were collected at the same time during spring 2011. This happened on 26th April 2011 (16:00–17:00 UTC). The vertical aerosol

profiles measured within this period are presented in Section 3.1.1. Here we just anticipate that these profiles were classified in Ferrero et al. (2016) as transitions from the so-called “negative gradient profiles class (NG)” to the “decoupled negative profile class (DNG)” (details in Section 3.1); these classes account together for the 68% of profiles occurring over Ny-Ålesund in spring making the chosen case study representative for Ny-Ålesund conditions. Moreover, on 26th April, Ny-Ålesund was influenced by a transport of Icelandic dust (as also happened in other days of April 2011). Details of dust transport are reported in a previous work (Moroni et al., 2018); Fig. S1 shows the back trajectories for the investigated case study. The dust composition is considered in Section 3.2.3 for the optical property calculations.

The methods for the aerosol characterization both along vertical profiles and at ground-level are detailed in Section 2.2, the lidar profiles in Section 2.3 and the optical properties calculations in Section 2.4.

2.2. Aerosol measurements and analyses

2.2.1. Tethered-balloon profiles

Vertical profile measurements were collected over Ny-Ålesund during the 2011–2012 campaign (ARCTICA2009 project); they have been extensively described in Ferrero et al. (2016) and Moroni et al. (2015, 2016). Here, we briefly resume the experimental set-up.

Vertical aerosol profiles were carried out utilizing a kytoon-shape tethered balloon (helium-filled, 8×3 m, 55.0 m^3 , 25 kg of payload, Fig. 1). The ascent/descent rates were set to $40.0 \pm 0.1 \text{ m/min}$; the maximum height reached during each flight was between 0.7 and 1.3 km with an average value of ~1.1 km.

The tethered balloon was equipped with: 1) a miniature Diffusion Size Classifier (miniDiSC, Matter Aerosol, (Fierz et al., 2011), 2) an Optical Particle Counter (OPC, 1.107 GRIMM, 0.25–32 μm , 6 s sampling time), 3) one micro-Aethalometer (microAeth® AE51, Magee Scientific, 60 s time resolution); however, on 26th April 2011 the inner memory encountered an electronic problem enabling to save just sporadic data points (thus ground EC ground data were used in the present work), 4) a miniaturized sampler (Sioutas SKC; 9 L/min, Leland Legacy pump, SKC, polycarbonate filters), 5) a meteorological station (Vaisala tethersonde TTS111, pressure, temperature, relative humidity, wind speed and wind direction; 1 s time resolution).



Fig. 1. Ny-Ålesund sampling site with the placement of KARL Lidar at the AWI-PEV Koldewey Station and the placement of Italian tethered balloon at the Gruvebadet (CNR) site.

The aerosol samples collected using the Sioutas sampling system were subjected to individual particle analyses by means of a SEM-EDS (Philips XL30 microscope equipped QUANTAX EDS microanalysis system with ESPRIT software for EDS spectra analysis of the elemental composition) as detailed in Moroni et al. (2018, 2016, 2015). Briefly, SEM data allowed to determine the shape factor of aerosol particles ($p^2/4\pi A$) in function of the perimeter (p) and the area of the geometrical projection of a particle (A ; within the image) in order to evaluate their degree of sphericity (shape factor is 1 for pure spherical particles; higher values are reached with increasingly irregular shapes (Ferrero et al., 2012).

Balloon-based meteorological data allowed the determination of the balloon altitude (hypometric equation) with high accuracy ($R^2 = 0.997$; slope = 0.999) as verified in Ferrero et al. (2016) with an independent system. The altitude accuracy is fundamental in this study in order to carefully match balloon and lidar data. In this respect, a gradient method has been applied to individuate the altitude of the aerosol stratifications (AS_h) (Ferrero et al., 2012, 2011a, 2011b, 2010; Sangiorgi et al., 2011; Di Liberto et al., 2012). The relationship between the AS_h and planetary boundary layer has been investigated in Ferrero et al. (2016) showing a good agreement with temperature and humidity profiles. In the present work, the AS_h is used to calculate a standardized height (H_s) calculated as follows:

$$H_s = \frac{z - AS_h}{AS_h} \quad (1)$$

where z is the height above ground. H_s assumes a value of 0 at the AS_h , and values of -1 and 1 at ground level and twice the AS_h , respectively. In this way, (Ferrero et al., 2016, 2014), H_s consider the relative position of each measured data point with respect to the AS_h allowing to exactly match balloon and lidar data collected above and below marked aerosol stratifications.

2.2.2. Ground-based data

Ground-based aerosol and meteorological measurements were carried out at the Gruvebadet laboratory (Fig. 1) which was equipped with a series of instruments aimed at measuring physical, chemical and optical properties of aerosol.

A Scanning Mobility Particle Sizer (TSI-Smps 3034, 54 size classes, 10–487 nm) and an Aerodynamic Particle Sizer (TSI-APS 3321, 52 classes, 0.5–20 μm) allowed the determination of the aerosol size distribution every 10 min (Giardi et al., 2016). The scattering coefficient was measured at 530 nm by a Radiance Research M903 nephelometer (1 s time resolution) and stored as minute averages. An absorption photometer (PSAP; three wavelengths: 467, 530, and 600 nm), was measuring the absorption coefficient with the same temporal resolution.

Aerosol samples were collected through two parallel TECORA SkyPost low-volume sampler (EN 12341; PM_{10} sampling head, flow 2.3 $\text{m}^3 \text{ h}^{-1}$; PTFE and Quartz fiber filters, $\varnothing = 47 \text{ mm}$). The first TECORA SkyPost collected PM_{10} sampled for 24 h on Teflon filters (Pall R2PJ047) for inorganic (Cl^- , NO_3^- , SO_4^{2-} , Na^+ , NH_4^+ , K^+ , Mg^{2+} , Ca^{2+}) and organic (oxalate, acetate, glycolate, formate and methanesulfonate) ions determination; the second TECORA SkyPost collected PM_{10} for 96 h on pre-fired Quartz microfiber filters (chm QF1 grade) to determine organic and elemental carbon. The organic matter (OM) was determined as 2.1 times OC (Turpin and Lim, 2001), typical for remote sites with a significant fraction of secondary aerosols. The analytical methodology, together with a quality assurance of analysis has been extensively discussed in Ferrero et al. (2016); thus we refer to this publication for further details which are also resumed in the Supplementary material.

2.3. Lidar data

The Lidar profiles in this work have been obtained at the "Koldewey Aerosol Raman Lidar" (KARL) located in the atmospheric observatory of

the German research base. The system is detailed in Hoffmann (2012). Briefly, it consists of a Nd:YAG laser which emits at three wavelengths: 355 nm, 532 nm and 1064 nm with 10 W at each wavelength and a repetition frequency 50 Hz. The backscattered light is collected by a 70 cm telescope, operating at a field of view 1.75 mrad. The elastically back-scattered light of the two colors mentioned above is recorded in two perpendicular states of polarization, parallel, and perpendicular to the polarization of the laser. Moreover, also the inelastically scattered light at N_2 molecules via the Raman effect is recorded at 387 and 607 nm from which the extinction is derived. The lidar data have a resolution of 7.5 m and 90 s. Above 600 m altitude, the system had a complete overlap (meaning that the laser beam is entirely inside the telescope's field of view).

The evaluation of the lidar data (backscatter and extinction) is performed via the method by Ansman et al. (1992). Further, the aerosol depolarization (i.e. the ratio of the aerosol backscatter perpendicular to parallel relative to the laser) was calculated (Freudenthaler et al., 2009). For our data, the estimated error was ~5% for the backscatter, ~25% for the extinction and ~0.8% for the depolarization.

For later use we also define the color ratio $CR_{(\lambda_1, \lambda_2)}$ as:

$$CR_{(\lambda_1, \lambda_2)} = \frac{\beta_{\lambda_1}^{aer}}{\beta_{\lambda_2}^{aer}} \quad (2)$$

where β_{λ}^{aer} represents the lidar backscattering coefficient due to the aerosol at the wavelength λ . The CR is a measure of the particles size with the limits $CR = 0$ for large particles and $CR = (\lambda_1 / \lambda_2)^4$ in the limit of Rayleigh scattering. Within the present work λ_1 and λ_2 were 355 and 532 nm, respectively.

2.4. Optical properties calculations

A Mie code base on the work of Bohren and Huffman (1983) was used to calculate the aerosol optical properties along vertical profiles to subsequently evaluate the agreement with the lidar backscattering ($\beta_{(\lambda)}$) coefficient.

In this respect, $\beta_{(\lambda)}$ profiles were calculated from vertical aerosol profile data as follows:

$$\beta_{(\lambda)} = \left(\frac{\lambda^2}{4\pi^2} \int_0^{D_p^{\max}} \left[\iint_{\Delta\Omega_{LDR}} i_{||(\theta, \phi, x, m)} \sin\theta d\theta d\phi \right] n_{D_p} dD_p \right) / \Delta\Omega_{LDR} \quad (3)$$

where λ is one of the three lidar wavelength (355, 532 and 1064 nm; Section 2.2), $i_{||(\theta, \phi, x, m)}$ is the parallel component of the Mie scattering function (the lidar used a parallel polarized light with respect to scattering plane generated by the source, the particle, and the telescope; Section 2.2), $\Delta\Omega_{LDR}$ is the solid angle between each aerosol particle and the lidar telescope, m and x are the aerosol complex refractive index and the size parameter (wavelength dependent) while, n_{D_p} represents the number-size distribution as a function of aerosol diameter D_p .

As contour parameters, the scattering coefficient ($b_{sca(\lambda)}$), the extinction coefficient ($b_{ext(\lambda)}$), the single scattering albedo (SSA) and the aerosol phase function (P) have also been calculated accordingly to the following equations (Seinfeld and Pandis, 2006; Crosbie and Davidson, 1985):

$$b_{sca/ext(\lambda)} = \int_0^{D_p^{\max}} \frac{\pi D_p^2}{4} Q_{sca/ext(m, x)} n_{D_p} dD_p \quad (4)$$

$$SSA_{\lambda} = \frac{b_{sca(\lambda)}}{b_{ext(\lambda)}} \quad (5)$$

$$P_{(\lambda,\theta,x,m)} = \frac{i(\theta, x, m)}{\frac{1}{2} \int_0^\pi i(\theta, x, m) \sin\theta d\theta} \quad (6)$$

where $Q_{sca/ext}$ are the scattering and extinction efficiencies, respectively.

The aforementioned optical parameters will be used in the [Results and discussion](#) section to control the quality of optical properties calculation by comparing with those measured at the Gruvebadet ground site. The calculation of aerosol optical properties (Eqs. (2)–(5)) requires accurate knowledge of the aerosol properties: refractive index, size-distribution, and shape.

In this respect, the aerosol refractive index calculation and the aerosol size distribution treatment are discussed in [Sections 2.4.1](#) and [2.4.2](#), respectively while, the applicability of the Mie theory, and thus the assumption of aerosol sphericity, is discussed in the result [Section 3.1](#). Here we just underline that the uses of Mie theory for particles may introduce uncertainties at least up to 15% ([Mishchenko et al., 1997](#)) and that the final results of the closure experiment (reported in [Section 3.2.3](#)) were far below this threshold.

2.4.1. Aerosol refractive index

The complex aerosol refractive index ($m = n + ik$) is a fundamental parameter in calculating the aerosol optical properties; moreover, it plays a central role in this work, as it is also used to correct the OPC size distribution by solving the “undersizing problem” ([Section 2.4.2](#)). Thus, it has a double, synergic effect, on the calculated backscattering coefficient (Eq. (3)).

In order to highlight the importance of a complete aerosol chemistry determination on m , three subsequent steps were used:

- Step-1, m of ambient aerosol was first estimated from the closest AERONET site (Hornsund; 77° 00' 04" N, 15° 33' 37" E) on 26th April 2011. The values of m at the lidar laser wavelengths were determined by linearly interpolating the AERONET data taken at different wavelengths (441, 674, 869, 1018 nm). This approach implies that m at 355 and 1064 nm were extrapolated. A such approach was successfully applied in [Balkanski et al. \(2007\)](#); in addition, it has to be noticed that the aim of using AERONET data, with a very simple linear interpolation, has just the aim produce a baseline level (“semi-quantitative”) of the lidar-tethered balloon comparison not with the aim to reach a perfect closure. This was done in order to highlight the need for further, and detailed aerosol chemical speciation. In this respect, the following, and more quantitative, approaches (2 and 3) were considered.
- Step-2, m of ambient aerosol was calculated from the ground-level chemical composition of aerosol, determined on PM₁₀ samples collected on 26th April 2011 ([Section 3.2.2](#)); as it will be shown in [Section 3.2.2](#) the chemical components analysed in PM₁₀ samples (water-soluble, EC/OM) did not explain 100% of the aerosol mass. Thus, for this second step, the unaccounted mass was neglected and only the role of water-soluble, EC/OM components was investigated; m was calculated from the measured PM₁₀ chemical composition ([Sections 2.1.2](#) and [3.2.2](#)) using the Bruggeman mixing rule (or effective medium approximation: EMA) ([Stier et al., 2007; Aspnes, 1982; Heller, 1965; Bruggeman, 1935](#)) as detailed below in this section.
- Step-3 aimed to treat the unaccounted mass of PM₁₀; in this respect the unaccounted mass of PM₁₀ was not neglected and assigned to the dust particles that reached Ny-Ålesund. The dust composition was based on the mineralogical phases detailed using balloon-based SEM-EDS data ([Section 3.2.3](#)); m for dust particles was again

calculated applying the Bruggeman mixing rule to the mineralogical phases as successfully done in [Balkanski et al. \(2007\)](#). Finally, dust particles were considered externally mixed to the EC/OM and water soluble components as suggested by [Moroni et al. \(2018, 2015\)](#); this approach was validated in previous works ([Ferrero et al., 2014, 2011a](#)).

Here below a detailed description of m computation is reported. As stated above, m (for step-2 and step-3) was calculated using the Bruggeman mixing rule that is as follows ([Ferrero et al., 2014; Stier et al., 2007; Aspnes, 1982; Heller, 1965; Bruggeman, 1935](#)):

$$\sum_{i=1}^n f_i \frac{\varepsilon_i - \varepsilon_{eff}}{\varepsilon_i + 2\varepsilon_{eff}} = 0 \quad (7)$$

where ε_{eff} is the complex effective dielectric constant of the mixture ($m_{eff} \approx \sqrt{\varepsilon_{eff}}$) and ε_i and f_i are the complex dielectric constant, and the volume fraction, respectively, of the i -th component, respectively. This approach does not consider a simple coated sphere assumption, but it is a part of more general mixing rule formulation resumed in [Aspnes \(1982\)](#). In this respect, the EMA overcomes the dilemma of the choice of a host medium ([Ferrero et al., 2014; Stier et al., 2007; Schuster et al., 2005; Bohren and Huffman, 1983; Aspnes, 1982; Heller, 1965](#)) but considers all the possible positions of each aerosol component (BC, dust, water-soluble materials, etc.) with respect to the others allowing simulating the real complexity of aerosols. Particularly, the EMA avoiding the risk of overestimating the imaginary part (k) of m , as instead happens using both the linear volume-average and the linear mass-average mixing rules ([Stier et al., 2007; Lesins et al., 2002](#)).

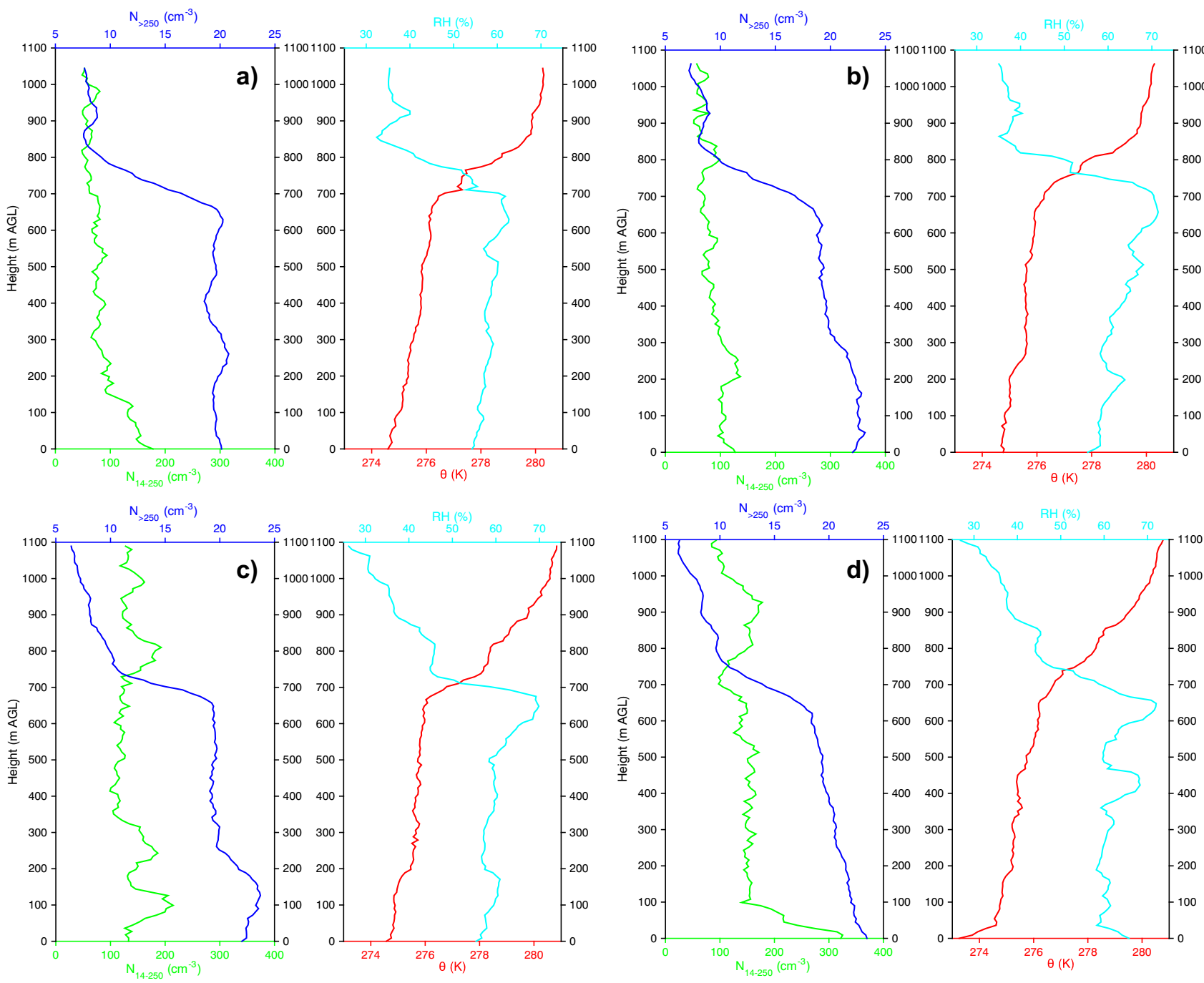
To apply Eq. (7), the volume fraction, as well as m , of each aerosol component are needed. Volume fractions were calculated using densities (ρ) of pure components ([Fierz-Schmidhauser et al., 2010; Kandler et al., 2007; Pesava et al., 2001; Chazette and Lioussse, 2001; Heller, 1965](#)). Refractive indexes values for pure components were chosen from the literature considering the state-of-the-art values ([Kandler et al., 2007; Hess et al. \(1998\); Bond and Bergstrom, 2006; Balkanski et al., 2007; Barthelmy, 2006; Ackerman and Toon, 1981](#)). This approach was yet successfully applied along vertical profiles, as reported in [Ferrero et al. \(2011a and 2014\)](#).

Finally, it noteworthy that the aerosol m varies in function of the hygroscopic growth of the aerosol that can be resumed as follows:

$$\frac{D_{wet}}{D_{dry}} = \left(\frac{1-RH}{1-DRH} \right)^{-\varepsilon} \quad (8)$$

where RH is the ambient relative humidity, D_{wet} is the aerosol diameter at ambient RH, D_{dry} is the dry aerosol diameter, DRH is Deliquescence Relative Humidity (DRH), and ε is the coefficient controlling the aerosol's hygroscopic growth. Thus, the aerosol experiences a hygroscopic growth if the ambient RH overreaches its DRH. In order to evaluate the water contribution to the m value, the DRH was estimated from the aerosol's chemical composition using the thermodynamic Aerosol Inorganic Model (E-AIM Model-IV), a state-of-the-art aerosol thermodynamic model for the H⁺-NH₄⁺-Na⁺-SO₄²⁻-NO₃⁻-Cl⁻-carboxylic acids-H₂O composition of the aerosol ([Zhang et al., 2000; Clegg et al., 1998](#)). The E-AIM model had been already used to predict aerosol DRH accurately ([Ferrero et al., 2013; Hueglin et al., 2005; Pathak, 2004](#)) and its validation using Aerosol Chamber measurements is detailed in [Ferrero et al. \(2015\)](#). DRH values for ambient RH are discussed in [Section 3.2.2](#).

Fig. 2. Vertical profiles of N_{14–250} (green line), N_{>250} (blue line), potential temperature (red line) and relative humidity (light blue line) measured from Gruvebadet on 26th April 2011 at a) 1607–1621 UTC; b) 1622–1636 UTC; c) 1643–1657 UTC; d) 1658–1712 UTC.



2.4.2. Aerosol size distribution

Information on the aerosol size distribution along height was obtained using the coupled miniDiSC – OPC from 14 nm (d_{50} cutoff of the miniDiSC) with an uncertainty of 7% and 16% for both miniDiSC and OPC data (Ferrero et al., 2016). The miniDiSC measures the total aerosol concentration from 14 nm. On the other side, the OPC provides the number size-distribution from 250 nm (lower detection limit) up to 32 μm , in terms of optical equivalent diameter which usually originates a “undersizing” effect.

The calculation of the aerosol optical properties requires a comprehensive knowledge of the entire number size distribution. Nevertheless, many authors (Randriamiarisoa et al., 2006; Guyon et al., 2003; Liu and Daum, 2008) report that uncertainties in nanoparticle concentrations may result in a ~2–4% error in the calculation of aerosol optical properties. Keeping in mind all the above considerations, we tried to recover the size distribution below 250 nm by using the shape of the number-size (n_{Dp}) measured at ground by the SMPS; the same reduced shape was applied to the full vertical profile data, with the only constraint to have an integral equal to the total aerosol concentration in the 14–250 nm range as provided by the miniDiSC.

Concerning the OPC, the undersizing effect originates from the calibration of the Grimm 1.107 OPC ($\lambda = 655 \text{ nm}$) with polystyrene latex spheres (PLS, $m = 1.58$ at 655 nm; Ma et al., 2003) whose refractive index has usually a higher real part compared to ambient aerosol (Section 3.2.1) (Guyon et al., 2003; Liu and Daum, 2008; Schumann, 1990). Thus the OPC classifies the aerosol in terms of optical equivalent diameter (the diameter of a sphere of polystyrene latex that scatters light as efficiently as the real particle in question; Howell et al., 2006) usually smaller than the real ones.

Thus, the “undersizing” issue was solved by correcting the OPC size channels in function of the ambient aerosol refractive index m , calculated for step-1, step-2 and step-3 as described in Section 2.3.2. In this respect, the OPC response function was computed both for PSL spheres (S_{PSL}) and for ambient aerosol (S_{AMB}) as follows (Baron and Willeke, 2005; Heyder and Gebhart, 1979):

$$S_{(\theta_0, \Delta\Omega_{\text{OPC}}, x, m)} = \frac{\lambda^2}{4\pi^2} \iint_{\Delta\Omega_{\text{OPC}}} i_{(\theta, \phi, x, m)} \sin\theta d\theta d\phi \quad (9)$$

where S is the partial light scattering cross section of the particle related to the specific optical design of the OPC, θ_0 is the mean scattering angle of the optical arrangement, $\Delta\Omega_{\text{OPC}}$ the receiver aperture, x the dimensionless size parameter, m the refractive index and $i_{(\theta, x, m)}$ the Mie scattering function (composed by the perpendicular and parallel components $i_{\perp(\theta, x, m)}$ and $i_{\parallel(\theta, x, m)}$, respectively). The receiver aperture of the OPC 1.107 consists of: 1) a wide angle parabolic mirror (121° , from 29.5° to 150.5° , $\theta_0 = 90^\circ$) that focuses scattered light on the photodetector located on the opposite side; 2) 18° of direct collected scattered light on the photodetector (from 81° to 99° , $\theta_0 = 90^\circ$) (Heim et al., 2008).

3. Results and discussion

Tethered balloon-based and lidar profiles were measured at the same time to perform a closure experiment along height. The obtained results are first discussed to introduce the vertical aerosol behaviour in relationship to the main atmospheric meteorological parameters and the PBL (Section 3.1). Then, the Mie theory is applied to the measured vertical aerosol profiles in order to calculate $\beta_{(\lambda)}$ and to compare them with the lidar signal at 355, 532 and 1064 nm (Section 3.2). All averaged data are reported from now as mean \pm mean standard deviation.

3.1. Vertical profile data

3.1.1. Tethered balloon – based aerosol data

As described in Section 2, four profiles collected on 26th April 2011 (16:00–17:00 UTC) were investigated for the present closure experiment.

The tethered balloon based profiles ($N_{<250}$ and $N_{>250}$) are reported in Fig. 2a–d together with the corresponding potential temperature (θ) and RH profiles. Fig. 2a–d highlights the presence of marked aerosol stratifications (AS_h) for $N_{>250}$ located on average at $698 \pm 9 \text{ m}$ (determined through the gradient method described in Section 2.2.3); across the AS_h $N_{>250}$ decreased by $-56.3 \pm 5.1\%$ going from $20.4 \pm 0.7 \text{ cm}^{-3}$ below the AS_h to $8.9 \pm 0.7 \text{ cm}^{-3}$ above it. This behaviour was not present for $N_{<250}$ which instead appeared quite constant along height ($123.7 \pm 15.9 \text{ cm}^{-3}$ below AS_h and $104.4 \pm 8.8 \text{ cm}^{-3}$ above it); only a ground-based plume present in the fourth profile with concentrations up to 325.2 cm^{-3} .

Interestingly, the vertical behaviour of the main meteorological parameters (θ , RH) was following that of $N_{>250}$ (Fig. 2a–d) marking a well defined thermodynamic structure in the vertical profile. In this respect, θ was characterized by a positive gradient with higher values above the AS_h ($279.3 \pm 0.5 \text{ K}$) than below it ($275.4 \pm 0.2 \text{ K}$) leading to a vertical $\Delta\theta$ of $+3.8 \pm 0.6 \text{ K}$. RH was characterized by a negative gradient with altitude leading to $20.3 \pm 3.5\%$ decrease across the AS_h ($40.4 \pm 3.0\%$ RH above the AS_h and $60.7 \pm 1.7\%$ below it). Finally, the wind was faster above it ($3.8 \pm 0.3 \text{ m s}^{-1}$) than below ($2.5 \pm 0.4 \text{ m s}^{-1}$) and experienced a clockwise rotation towards the north direction (Fig. 3a–b). Finally, in the fourth profile (Fig. 2d), a ground-based plume of $N_{<250}$ appeared below 100 m and was constrained there by a small ground-based θ inversion ($\Delta\theta: +1.5 \text{ K}$). In this respect, ground SMPS data (Fig. S2) clearly showed a doubling of nanoparticle concentration ($D_p < 100 \text{ nm}$) in the last profile compared to the others.

The aforementioned results describe a common situation over Ny-Ålesund, in which a transition from the so-called “negative gradient profiles class (NG)” to the “decoupled negative profile class (DNG)” (negative aerosol gradients are located at different altitude; Section 1) appears. As reported in Ferrero et al., 2016, NG + DNG profiles account together for 68% of cases over Ny-Ålesund making the present Lidar-Balloon closure experiment an important representative case study. More details concerning ground-based aerosol plumes, mostly related to the secondary aerosol formation, are reported in Ferrero et al. (2016) and are not discussed here as they are beyond the aim of the present closure work. In the following section (Section 3.1.2) a qualitative comparison with lidar data is discussed while the quantitative comparison is reported in Section 3.2.

3.1.2. Lidar data: qualitative comparison with aerosol profiles

A first qualitative comparison of the vertical behaviour between β_{532} and $N_{>250}$ was carried out in function of the standardized altitude H_s aiming to verify the presence of the necessary conditions to perform a quantitative closure experiment. The comparison is reported in Fig. 4a–d. The lidar signal shows first an earlier increase of $\beta_{(\lambda)}$ with height that was merely due to the completion of the lidar overlapping (until ~600 m); instead, the most interesting feature is given at higher altitudes where β_{532} and $N_{>250}$ are shaped in the same way following the meteorological behaviour described in the previous section (Section 3.1.1). When considering their absolute values, β_{532} experienced a more intense decrease with altitude ($71.2 \pm 8.5\%$: from $2.01 \pm 0.09 \text{ Mm}^{-1} \text{ sr}^{-1}$ below the AS_h to $0.57 \pm 0.13 \text{ Mm}^{-1} \text{ sr}^{-1}$ above it) than those observed for $N_{>250}$ ($56.3 \pm 5.1\%$: from $20.4 \pm 0.7 \text{ cm}^{-3}$ below the AS_h to $8.9 \pm 0.7 \text{ cm}^{-3}$ above it). This difference is due to the fact that this comparison does not take yet into account both the conversion of aerosol concentration into optical properties and the changing distance from the lidar telescope with altitude that influence the value of $\Delta\Omega_{\text{LDR}}$ (Eq. (3)). An altitude dependent variation of $\Delta\Omega_{\text{LDR}}$ influences the amount of

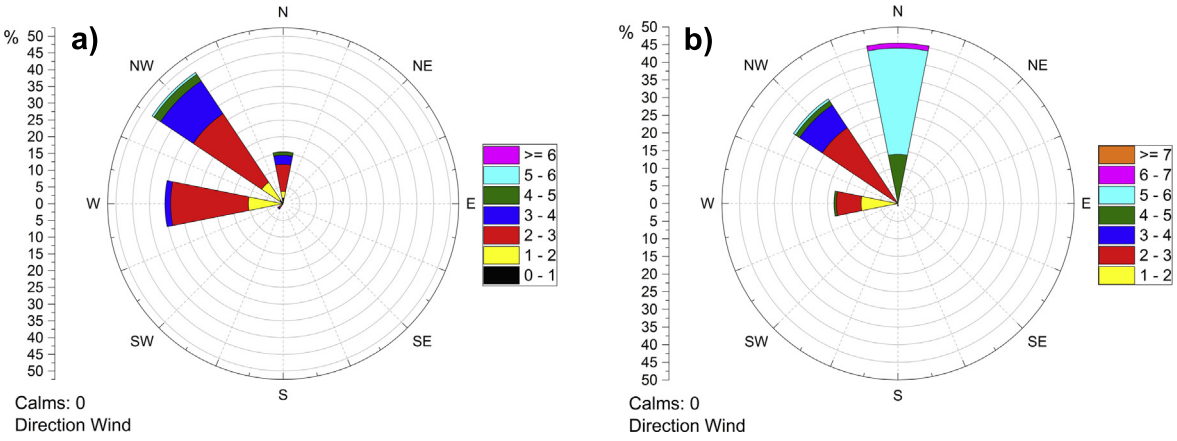


Fig. 3. Windrose obtained from the measured wind speed on the tethered balloon both below the AS_h (a) and above it (b).

backscattered radiation into the solid angle observed by the telescope; moreover, this dependence is related to the phase function (P) of each aerosol particle. However, from a qualitative point of view, Fig. 4a-d clearly shows the presence of the first necessary

conditions to perform a good closure experiment: β_{532} and $N_{>250}$ were shaped in the same way along height.

In addition to this, $\beta_{(\lambda)}$ (355 and 532 nm) allowed the calculation of the lidar color ratio CR (β_{355}/β_{532} ; Section 2.2; Fig. 4a-d) profiles.

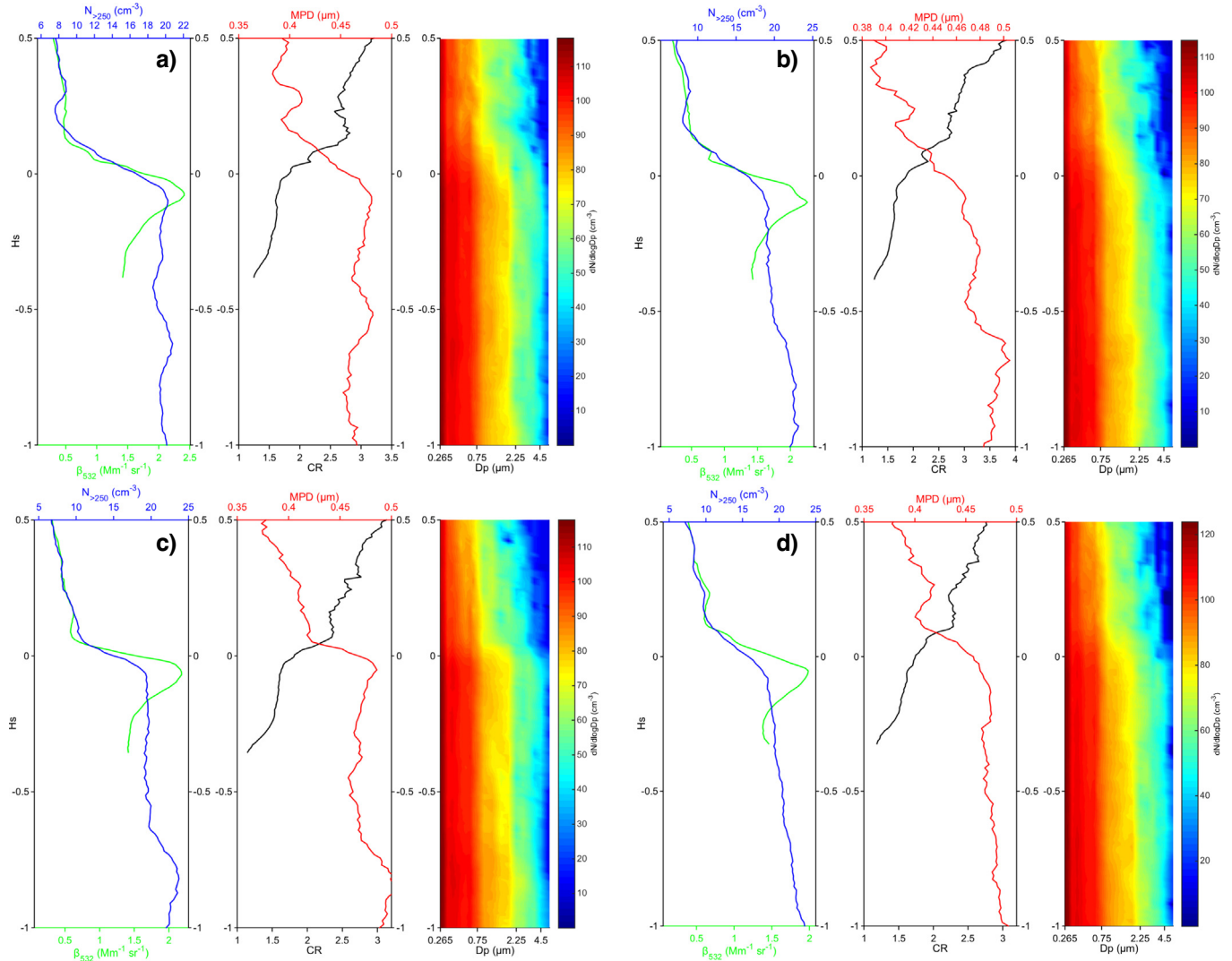


Fig. 4. Vertical profiles of β_{532} (green line), $N_{>250}$ (blue line), MPD (red line), CR (black line) and OPC number size distribution (colored counter plot) measured from Gruvebadet on 26th April 2011 at a) 1607–1621 UTC; b) 1622–1636 UTC; c) 1643–1657 UTC; d) 1658–1712 UTC.

They exhibited an increase with altitude with a marked positive step at $H_s = 0$ in correspondence of the AS_h. As stated in Section 2.2 a CR increase is expected at the decrease in the aerosol size. Thus, the mean particle diameter (MPD, in terms of optical equivalent diameter) was calculated along height from OPC data as follows (Ferrero et al., 2012):

$$MPD = \frac{\sum_i N_{(i)} D_{p(i)}}{\sum_i N_{(i)}} \quad (10)$$

where $N_{(i)}$ and $D_{p(i)}$ are the number concentration and the optically equivalent diameter of the i-th OPC size class.

Fig. 4a-d show that the CR experienced a $+57.0 \pm 10.9\%$ increase above the AS_h (going from 1.65 ± 0.03 to 2.60 ± 0.18), while the corresponding aerosol MPD profiles evidenced a decrease of $-14.8 \pm 1.9\%$ (from $0.48 \pm 0.01 \mu\text{m}$ below the AS_h to $0.40 \pm 0.01 \mu\text{m}$ above it). This reduction in MPD with altitude is the consequence of the loss of larger particles above the AS_h, as highlighted for the four profiles in Fig. 4a-d. Thus, a second necessary condition for a closure experiment was satisfied: an agreement between the optical response of the lidar and the aerosol size distribution with altitude.

Finally, the applicability of the Mie theory, and thus the assumption of aerosol sphericity, is discussed. This assumption results first from the lidar observations; Fig. 5 reports the contour plot of lidar depolarization profiles measured on 26th April 2011. The depolarization reached negligible values ($<1 \pm 0.8\%$) below 1.1 km (the maximum altitude reached by the tethered balloon during the same day). The low depolarization values imply that the aerosol particles above the measuring station optically acted as spherical supporting the use of the assumption of sphericity as reasonable for the context of this application. This is also in agreement with SEM observation of dust impacting Ny-Ålesund in April, both at ground and along vertical profiles, that showed shape factor frequency distribution peaking between 1 and 1.25 (1 is for pure spherical particles) with 42% and 27% of frequency, respectively. Moreover, 98% and 80% of particles were characterized by shape factors below 2 (Moroni et al., 2018, 2015).

3.2. Closure experiment

In order to introduce the closure experiment, it is important to note the high level of similarity among the four profiles under investigation (see Figs. 2a-d and 4a-d). Given this observation, hereinafter the four profiles were averaged as a function of H_s considering the relative position of each measured data point with respect to the AS_h; this approach allows to show altogether the results of the closure experiment in function of the different wavelengths and the different treatment of m and size of the aerosol (as described in Sections 2.3.1 and 2.3.2). The resulted averaged profile for $N_{<250}$, $N_{>250}$, θ , RH, β_{532} and CR are reported in Fig. 6 from a $H_s > -0.1$, a value over which the lidar overlapping is ensured. Here below, the closure experiments for step-1, step-2 and step-3 are reported and discussed (Sections 3.2.1, 3.2.2 and 3.2.3).

3.2.1. Step-1: AERONET based refractive index

Previous sections underlined the agreement between tethered balloon aerosol data and lidar signal from a qualitative point of view. In order to match them quantitatively, a first step (as stated in Section 2.3.1), was done using m of ambient aerosol estimated from the AERONET data at the Hornsund site. This step aimed to produce a baseline level (semi-quantitative) in the lidar-tethered balloon comparison; m at the lidar laser wavelengths (355, 532 and 1064 nm) were: $1.536 + 0.003i$, $1.544 + 0.004i$ and $1.545 + 0.008i$, respectively. The following OPC size channels corrected at the OPC laser wavelength (655 nm, m : $1.551 + 0.005i$) are reported in Table 1.

β_{355} , β_{532} and β_{1064} were computed following Eq. (3) and compared with the corresponding lidar profiles (Fig. 7a-c). The vertically averaged β_{355} , β_{532} and β_{1064} obtained from Mie calculations were 0.41 ± 0.07 ,

0.42 ± 0.08 and $0.28 \pm 0.06 \text{ Mm}^{-1} \text{ sr}^{-1}$, showing an underestimation with respect to the corresponding lidar data (vertical averages: 1.60 ± 0.22 , 0.75 ± 0.16 and $0.31 \pm 0.08 \text{ Mm}^{-1} \text{ sr}^{-1}$). Notably, the underestimation was higher for the lowest wavelength (355 nm) and lowest for the highest wavelength (1064 nm) (Fig. 7a-c). The root-mean-squared error (RMSE) was 1.33, 0.44 and $0.11 \text{ Mm}^{-1} \text{ sr}^{-1}$ (355, 532 and 1064 nm) leading to a not-accounted fraction of β_{355} , β_{532} and β_{1064} of 75, 44 and 11%, respectively.

This effect was also highlighted by the scatter-plots between balloon-based Mie calculation and lidar backscattering data (Fig. 8a-c) in which the slopes were lower than one (0.312, 0.511 and 0.681, respectively) while intercepts were close to zero, avoiding the presence of fixed biases. It is noteworthy, however, that the correlation values were very high (R^2 of 0.991, 0.988, 0.989, respectively); despite the negative bias, β_{355} , β_{532} and β_{1064} calculated with Mie theory were shaped vertically in the same way of lidar data (Fig. 8a-c). In order to control the quality of the calculation performed, the aerosol phase function $P_{(\lambda, \theta)}$ was computed at the same AERONET wavelengths (441, 674 and 896 nm), vertically averaged and compared with the columnar AERONET $P_{(\lambda, \theta)}$ estimations. The comparison is reported in Supplemental material (Fig. S3) and showed a well reproduced $P_{(\lambda, \theta)}$ highlighting that the β_{355} , β_{532} , and β_{1064} underestimation could be due to factors other than Mie approach (assumption already discussed in Sections 2.3 and 3.1.2). Mainly, the complex refractive index m was roughly estimated by AERONET at another site and, most important, this was a columnar refractive index. Thus, the following two steps (Sections 3.2.2 and 3.2.3) are dedicated to including the aerosol chemistry for a more precise quantification.

3.2.2. Step-2: water-soluble, EC/OM chemistry-based refractive index

In order to reach a more accurate closure with lidar data the PM₁₀ chemical composition was considered (Section 2.1.2) (Fig. 9a). Fig. 9a shows that 45.05% of chemical composition was explained by water-soluble inorganic ions, mainly dominated by NaCl (35.39%) from sea spray, followed by 9.46% of OM and negligible EC in agreement with data reported in Ferrero et al. (2019, 2016). Fig. 9a also highlights that the unaccounted fraction was very high (up to 45.42%) compared to the average value of the NG-DNG profiles during spring 2011 campaign (31.92%, Ferrero et al., 2016). This indicates that the composition of this sizeable aerosol fraction should not be neglected in the optical property calculation. However, for this second step, only the water-soluble, EC/OM contribution was considered and used both to calculate m (-Section 2.3.1) and to correct the OPC size distribution for the “undersizing” (Section 2.3.2).

In this respect, aerosol affinity for water (and its effect on m) was investigated using the thermodynamic Aerosol Inorganic Model (E-AIM Model-IV, Section 2.3.1). The DRH was determined using the aerosol chemical composition reported in Fig. 9a, at 271 K, which was the average temperature along vertical profiles. DRH was finally compared with the RH vertical profiles to determine the hygroscopic growth following Eq. (7). The E-AIM Model-IV output is reported in Fig. S4 and shows a DRH at 74% RH. It is noteworthy that no-one of the four RH profiles reported in Figs. 2a-d and 6 overreached 70% RH, thus leading to a dry aerosol condition. Thus, m was calculated using the Bruggeman mixing rule (Eq. (6)) based on the measured chemical composition. Results were as follows: $1.515 + 0.002i$, $1.510 + 0.002i$ and $1.486 + 0.006i$, at 355, 532 and 1064 nm, respectively. They appeared characterized by a lower real part compared to m values estimated by AERONET in the previous Section 3.2.1. As a result, the OPC size channels corrected at the OPC laser wavelength (655 nm, m : $1.504 + 0.003i$; Table 1) were higher than those corrected using the AERONET m , due to an enhanced OPC “undersizing”.

From the data above, β_{355} , β_{532} and β_{1064} were computed following Eq. (2) and compared with the corresponding lidar profiles in Fig. 7d-f. If vertically averaged, β_{355} , β_{532} , and β_{1064} (0.38 ± 0.06 , 0.35 ± 0.07 and $0.17 \pm 0.03 \text{ Mm}^{-1} \text{ sr}^{-1}$, respectively) were considerably lower both of

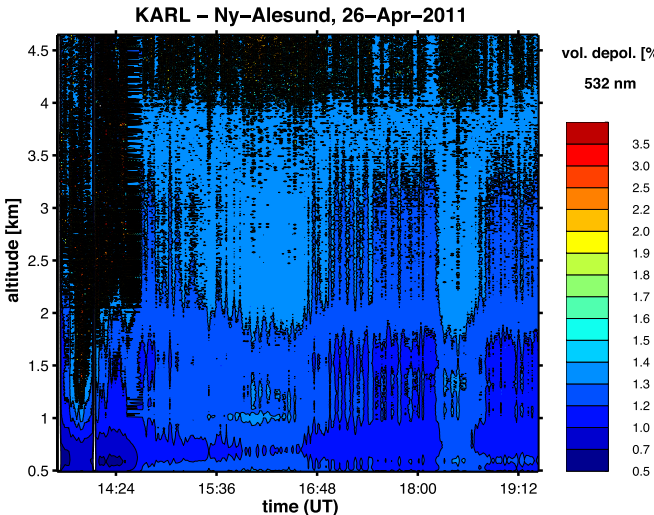


Fig. 5. KARL-lidar depolarization volume in percentage during the investigated study case on 26th April 2011.

lidar data (vertical averages: 1.60 ± 0.22 , 0.75 ± 0.16 and $0.31 \pm 0.08 \text{ Mm}^{-1} \text{ sr}^{-1}$) and also of the estimation based on AERONET m reported in the previous section (Section 3.2.1).

Similarly, to previous AERONET based calculations, the underestimation was higher for the lowest wavelength (355 nm) and lowest for the highest (1064 nm) (Fig. 7d-f) with a RMSE of 1.36, 0.51 and $0.32 \text{ Mm}^{-1} \text{ sr}^{-1}$. This corresponded to a not-accounted fraction of β_{355} , β_{532} and β_{1064} of 76, 53 and 45%, respectively. Even in this case, balloon-based Mie calculation and lidar backscattering data were highly correlated (R^2 of 0.989, 0.990 and 0.990) and thus vertically shaped in the same way (Fig. 8d-f). However, in this case, slopes were lower than one (0.285, 0.452 and 0.412, respectively) and lower than those previously obtained using AERONET data. Even in this case, intercepts were close to zero.

It is noteworthy that a slight change in m has a double (synergic) effect on the closure exercise. Notably, a lower real part (with very similar imaginary ones), not only decreases the scattering by itself but also (and most important for the present work) increases the size-corrected OPC

channels (Table 1) leading to lower backscattering around 180° due to a particle size effect. In this respect, the OPC size channels (corrected for the chemical composition) below $1 \mu\text{m}$ (the most concentrated and active in the backscattering region) were $+18.2 \pm 1.4\%$ larger than the original ones and $+12.2 \pm 1.1\%$ larger than those corrected for AERONET m during the Step-1. In order to quantify this size effect on $\beta(\lambda)$, the aerosol phase function $P_{(\lambda,\theta)}$ was computed at the lidar wavelengths (355, 532 and 1064 nm), vertically averaged and compared with the aerosol phase function $P_{(\lambda,\theta)}$ computed at the same wavelengths but using the AERONET m from the previous section (Section 3.2.1). The comparison of $P_{(355,\theta)}$, $P_{(532,\theta)}$, $P_{(1064,\theta)}$, is reported in Fig. 10a-c. As it is possible to observe, $P_{(\lambda,\theta)}$, obtained using m derived from the chemical composition, showed lower values close to 180° (especially at 532 and 1064 nm) compared to those obtained by AERONET.

As a conclusion, the results obtained with this step of calculations suggest the presence in the atmosphere of aerosol components other than that measured by classical chemical analysis in PM_{10} samples; their presence is suggested both by the higher real part in the AERONET refractive index and by the high unaccounted aerosol fraction (45.42%; Fig. 9a). In this respect, a careful treatment of the unaccounted fraction is needed and is investigated in the following section (Section 3.2.3).

3.2.3. Step-3: the role of dust composition

The third step aimed to reach a more accurate closure with lidar data including the unaccounted fraction (Fig. 9a-b). An important indication on how to treat the unaccounted fraction comes from the recent work of Ferrero et al. (2019) in which it has been demonstrated that the high unaccounted fraction is a specific feature of PM measured in Ny-Ålesund compared to that observed over the Arctic ocean and is an indication of the presence of mineral compounds (related to dust both locally originated and long range-transported) as described in Moroni et al. (2018, 2016, 2015). Particularly, results reported in the aforementioned papers, showed that on 26th April 2011, air masses travelled over Iceland, close to the surface, before reaching Ny-Ålesund. The main constituents in weight% were sheet silicates (68.0%), gypsum (14.6%), rutile (7.6%), Feldspars (6.2%), dolomite (1.7%), hematite (1%) and quartz (0.9%).

Thus, replacing the unaccounted fraction with the aforementioned mineralogical data leads to the final chemical composition reported in

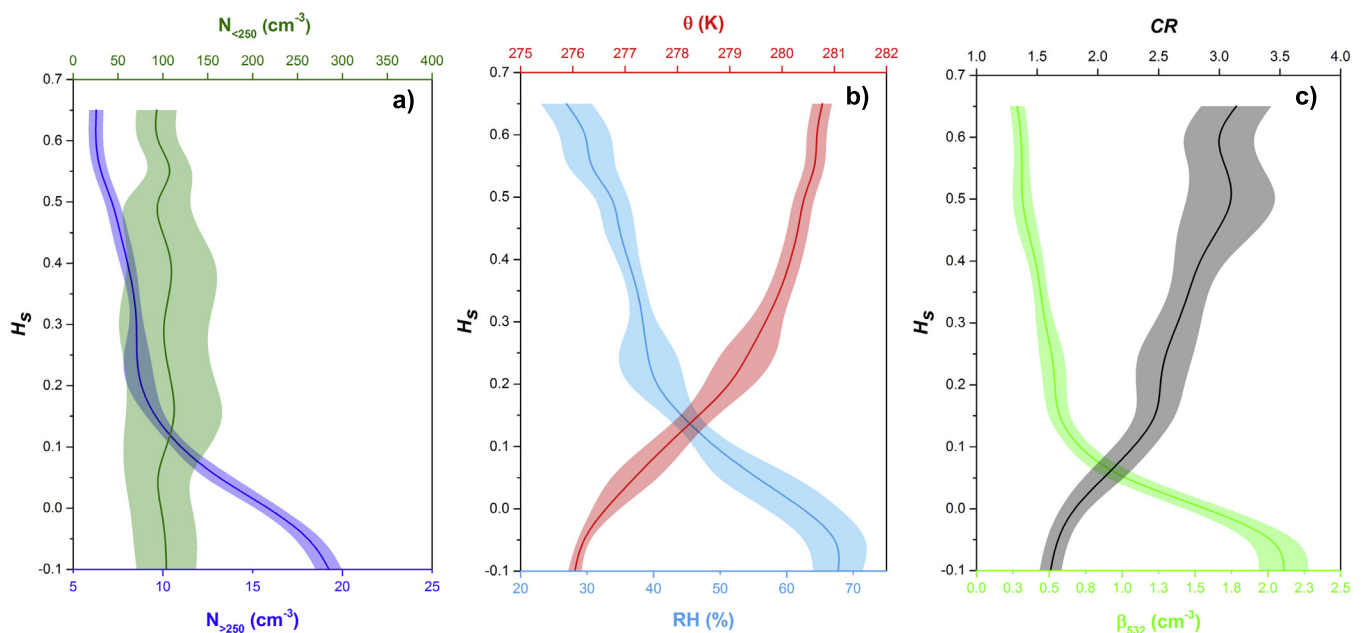


Fig. 6. Averaged vertical profiles of: a) $N_{<250}$ (blue line), $N_{>250}$ (olive line); b) potential temperature (red line) and relative humidity (light blue line); c) β_{532} (light green line) and CR (black line) measured from $H_s > -0.1$.

Table 1

Original size channels of OPC Grimm 1.107 calibrated with PSL spheres (left side) and corrected (right side) for m obtained by Aeronet, by ground PM₁₀ chemistry and by dust composition.

Instrument size (μm)	OPC channel	Ambient size (μm)		
		PLS	Aeronet	PM ₁₀ chemistry
1	0.25	0.26	0.28	0.24
2	0.28	0.29	0.32	0.27
3	0.30	0.31	0.34	0.29
4	0.35	0.36	0.40	0.34
5	0.40	0.42	0.48	0.38
6	0.45	0.47	0.54	0.43
7	0.50	0.52	0.58	0.48
8	0.58	0.62	0.75	0.56
9	0.65	0.71	0.79	0.62
10	0.70	0.73	0.82	0.68
11	0.80	0.85	0.97	0.79
12	1.00	1.12	1.19	0.98
13	1.30	2.00	1.80	1.66
14	1.60	2.16	1.86	1.82
15	2.00	2.37	2.34	2.15
16	2.50	2.79	3.16	2.48
17	3.00	3.80	3.67	3.16
18	3.50	4.62	4.57	3.76
19	4.00	5.25	5.13	4.27
20	5.00	6.17	6.03	5.01
21	6.50	9.77	9.33	7.16
22	7.50	10.84	10.35	7.94
23	8.50	12.74	12.02	8.71
24	10.00	16.79	15.31	10.47
25	12.50	23.71	21.13	13.96
26	15.00	30.90	27.86	16.98
27	17.50	38.02	35.48	20.18
28	>20.00	>44.67	>43.65	>23.44

Fig. 9b. The SEM-EDS data gave the mass abundance of different minerals in relative ratio one to each other; thus, in order to replace the unaccounted fraction (45.42%) with mineralogical data, it was assumed that the total unaccounted fraction was due to measured dust aerosol, and the relative proportions of the mass abundance of different minerals obtained by SEM-EDS were scaled and kept constant in order to result in a sum equal to the unaccounted fraction (45.42%). Finally, it is to be noticed that **Fig. 9b** shows Na⁺ and SO₄²⁻ together with gypsum. Thus, the sea-salt origin of both Na⁺ and SO₄²⁻ was investigated (as done in Ferrero et al. (2016); see Supplementary material) showing that at ground level the Na⁺ and SO₄²⁻ of crustal origin were negligible compared to the sea-salt originated ones.. In this respect, Moroni et al. (2015) showed (using SEM-EDS) that the sea-salt particle contribution decreased with altitude, where the mineral components became more important. For this reason, when determining the optical aerosol properties along the vertical column (below and above the boundary layer), both the ionic contribution of Na⁺ and SO₄²⁻ and that of gypsum (determined via SEM-EDS) were considered at the same time as externally mixed.

Following the aforementioned considerations, mineralogical data allowed the calculation of the m of dust by using the Bruggeman mixing rule (Eq. (7)); then, as discussed in Section 2.3 the dust fraction was considered externally mixed with respect to the water-soluble, EC/OM fractions (step-2) in calculating $\beta_{(\lambda)}$ using Eq. (3).

From Eq. (7), m of dust were $1.704 \pm 0.001i$, $1.650 \pm 0.001i$, and $1.594 \pm 0.001i$, at 355, 532 and 1064 nm, respectively; they were characterized by a higher real part compared to values estimated both by AERONET (Section 3.2.1) and by the simple water-soluble, EC/OM chemistry (Section 3.2.2).

From the data above, β_{355} , β_{532} and β_{1064} were computed following Eq. (3) and compared with the corresponding lidar profiles (**Fig. 7g-i**). If

vertically averaged, β_{355} , β_{532} and β_{1064} were 1.45 ± 0.30 , 0.69 ± 0.15 and $0.34 \pm 0.08 \text{ Mm}^{-1} \text{ sr}^{-1}$, now matching with the lidar vertical averages: 1.60 ± 0.22 , 0.75 ± 0.16 and $0.31 \pm 0.08 \text{ Mm}^{-1} \text{ sr}^{-1}$, respectively. A slight underestimation remains for the lowest wavelength (355 nm). The RMSE were 0.36, 0.08 and $0.04 \text{ Mm}^{-1} \text{ sr}^{-1}$, corresponding to a not-accounted fraction of β_{355} and β_{532} of 9 and 7%, while β_{1064} was overestimated of 9%. As already observed for step-1 and step-2, balloon-based Mie calculation and lidar backscattering data were highly correlated (R^2 of 0.992, 0.992 and 0.994, **Fig. 8g-i**). Most important, in this case slopes were close to one (1.368, 0.931 and 0.977, respectively); the slope of β_{355} was higher than one only because the 9% underestimation was mainly due to above AS_H data (**Fig. 8g**) giving the only case in the closure experiment with an intercept in the linear regression significantly different from zero (-0.742 ; **Fig. 8g**).

The good agreement obtained in this step, was due to the synergic effect of higher real part of m and the consequent decrease of the size-corrected OPC channels (**Table 1**). Particularly, the OPC size channels corrected at the OPC laser wavelength (655 nm, m : $1.623 \pm 0.001i$; **Table 1**) were the lowest ones, and also lower than the original OPC size channel; this case represents a rare case of OPC “oversizing” in which the ambient aerosol had a refractive index higher than that used for OPC calibration (1.58; Section 2.3.2). In this respect, the OPC size channels below 1 μm (the most concentrated and active in the backscattering region), corrected for the dust composition, were $-3.0 \pm 0.2\%$ lower than the original ones and $-17.9 \pm 1.0\%$ lower than those corrected for just the water-soluble, EC/OM components during the Step-2. In this respect, the aerosol phase function $P_{(\lambda,\theta)}$ was computed at the lidar wavelengths (355, 532 and 1064 nm), vertically averaged and compared with the aerosol phase function $P_{(\lambda,\theta)}$ computed at the same wavelengths both using the AERONET m (Section 3.2.1) and the water-soluble, OM/EC based m . (**Fig. 10a-c**). As it is possible to observe, $P_{(\lambda,\theta)}$, obtained using m derived only from the dust, showed the highest values close to 180° within the field of view of the lidar telescope.

A final validation of the obtained results comes from a comparison of the scattering coefficient ($b_{sca(\lambda)}$) and the single scattering albedo (SSA) measured at Gruvebadet (ground-level) and the AERONET Hornsund site (columnar).

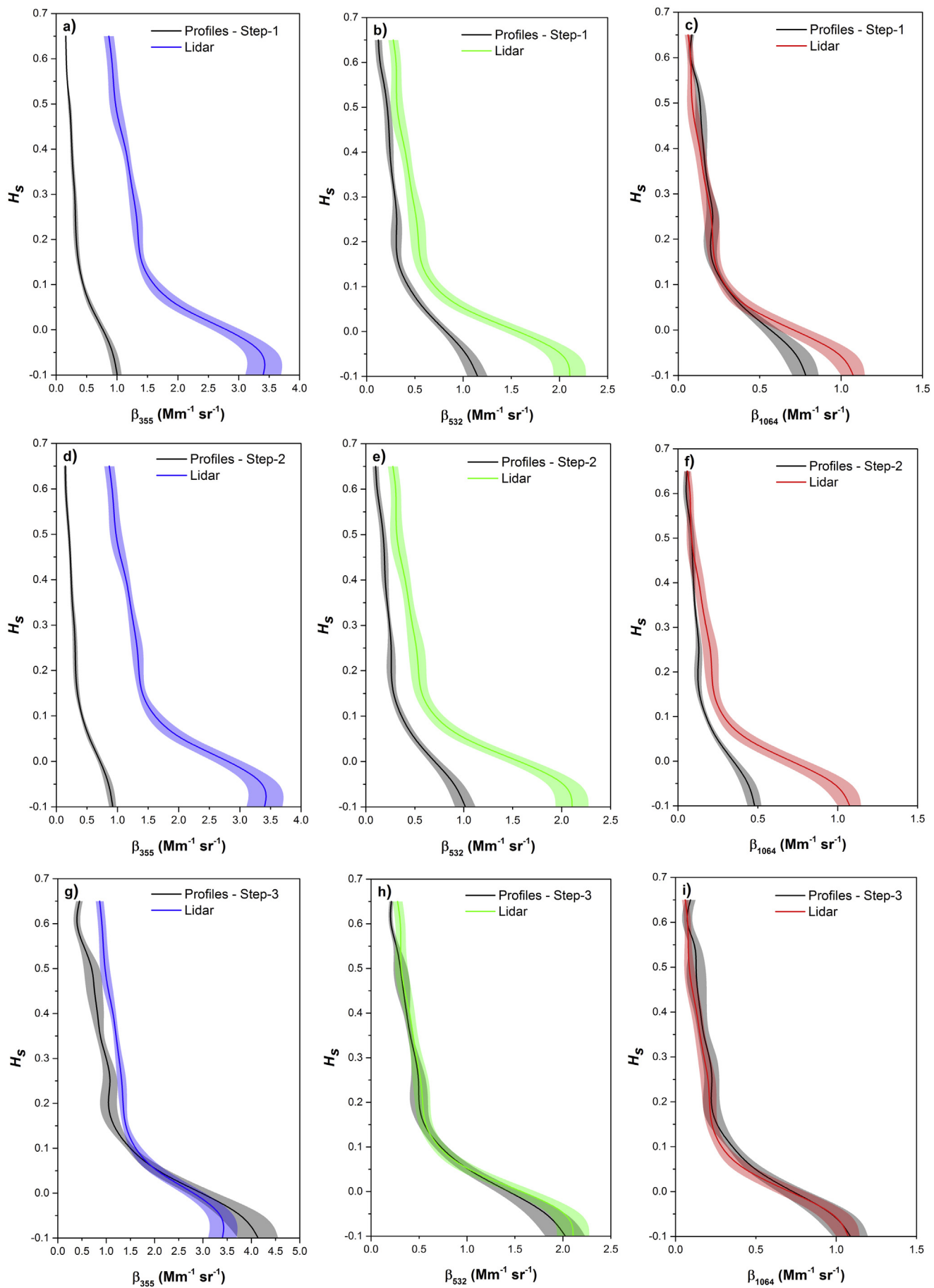
Starting from the ground, $b_{sca(532)}$ determined by Mie calculations was $11.56 \pm 1.25 \text{ Mm}^{-1}$ entirely in keeping with $b_{sca(530)}$ of $11.13 \pm 1.24 \text{ Mm}^{-1}$ determined at the same time by the nephelometer at Gruvebadet. For what concern the ground SSA₍₅₃₂₎, determined by Mie calculations, it was 0.972 ± 0.001 , slightly higher than that obtained at Gruvebadet (0.913 ± 0.002) at 530 nm. However, if vertically averaged along the atmospheric column, SSA₍₅₃₂₎, determined by Mie calculations, was 0.974 ± 0.001 in keeping with columnar AERONET data in Hornsund on 26th April 2011: 0.965 ± 0.007 and 0.957 ± 0.011 at 441 and 647 nm, respectively.

4. Conclusions

A closure experiment was carried out by comparing optical properties derived from Lidar data and those calculated from aerosol properties measured along vertical profiles using the tethered balloon platform. Data used for the closure experiment were collected on 26th April 2011, a case study impacted by both Arctic Haze and Icelandic dust transport.

The closure experiment was set up in three subsequent steps: the first one in which refractive indexes of aerosol were determined from the nearest AERONET station (Hornsund), the second one in which the aerosol refractive index was determined from the chemical composition, routinely measured (ionic water-soluble components, EC/OM) at

Fig. 7. Comparison between the backscattering vertical profiles measured by lidar at 355, 532 and 1064 nm and those calculated using m : from Aeronet (Step-1, a-c), from PM₁₀ chemistry neglecting the unaccounted mass (Step-2, d-f) and from PM₁₀ chemistry considering the unaccounted mass as due to Icelandic dust (Step-3, g-i).



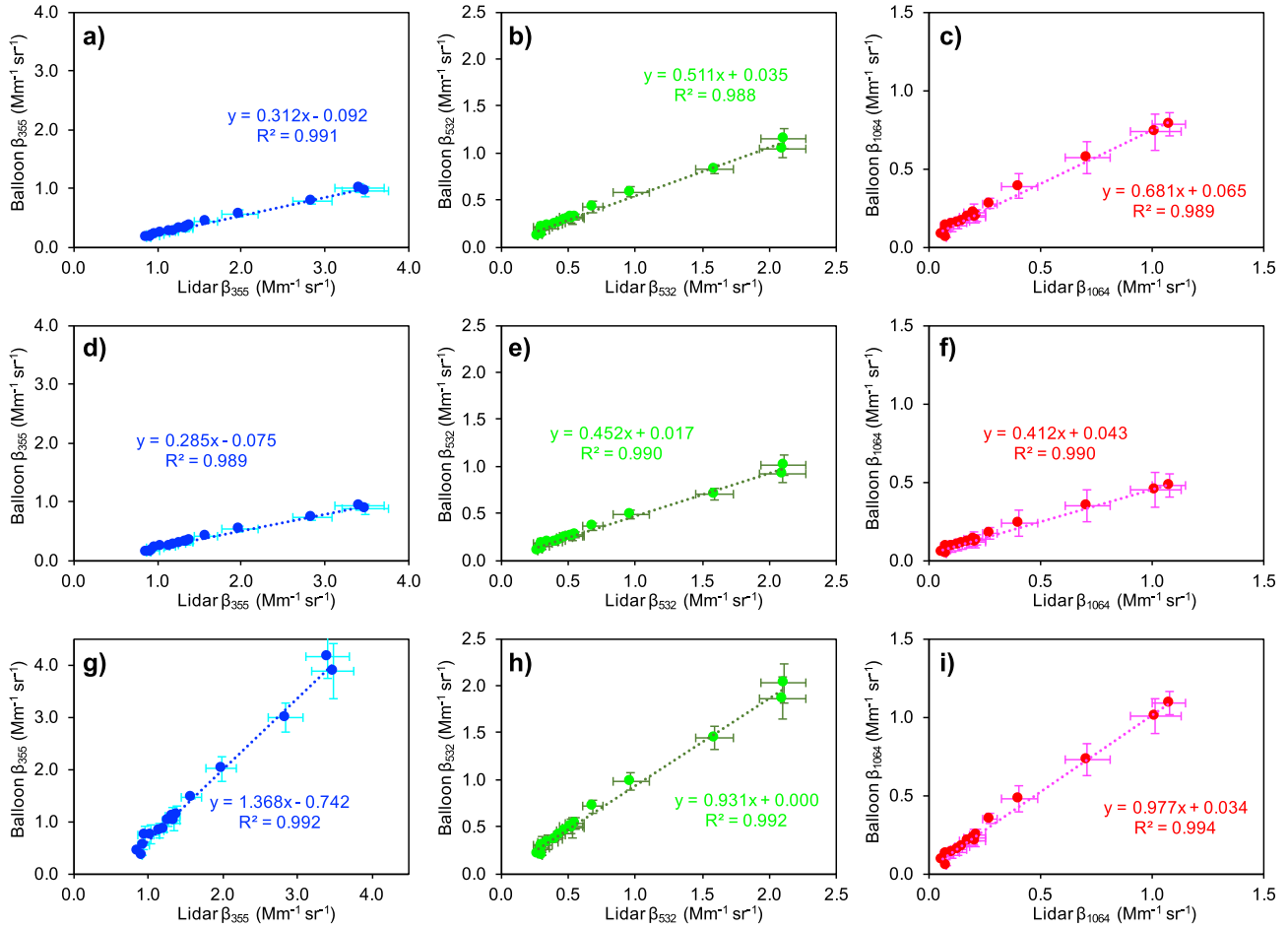


Fig. 8. Linear correlation between the backscattering vertical profiles measured by lidar at 355, 532 and 1064 nm and those calculated using m : from Aeronet (Step-1, a-c), from PM_{10} chemistry neglecting the unaccounted mass (Step-2, d-f) and from PM_{10} chemistry considering the unaccounted mass as due to Icelandic dust (Step-3, g-i). Data points represent averages of backscattering coefficients along H_s with a 0.05 step.

ground, and finally, the third one accounting for the Icelandic dust properties in synergy with the ionic components, the EC and OM.

Following these approaches, it was determined that the backscattering coefficients computed from balloon data considering the columnar AERONET refractive index or that estimated only from the chemical composition routinely measured (ionic water-soluble components,

EC/OM) led to an underestimation of the lidar signal up to 76, 53 and 45%, at 355, 532 and 1064 nm, respectively.

Instead, if the dust composition is accounted for, the underestimation disappeared and the vertically averaged, backscattering coefficients (1.45 ± 0.30 , 0.69 ± 0.15 and $0.34 \pm 0.08 \text{ Mm}^{-1} \text{ sr}^{-1}$, at 355, 532 and 1064 nm) were found in good accordance with the lidar ones: $1.60 \pm$

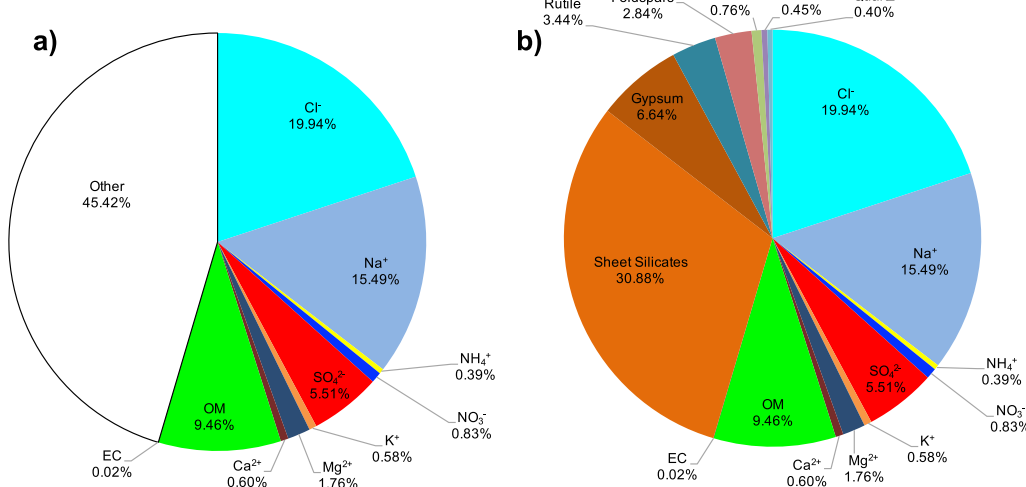


Fig. 9. Chemical composition measured at the ground on PM_{10} sample (a) and chemical composition of the same PM_{10} sample considering the unaccounted mass as due to dust mineralogical phases (b).

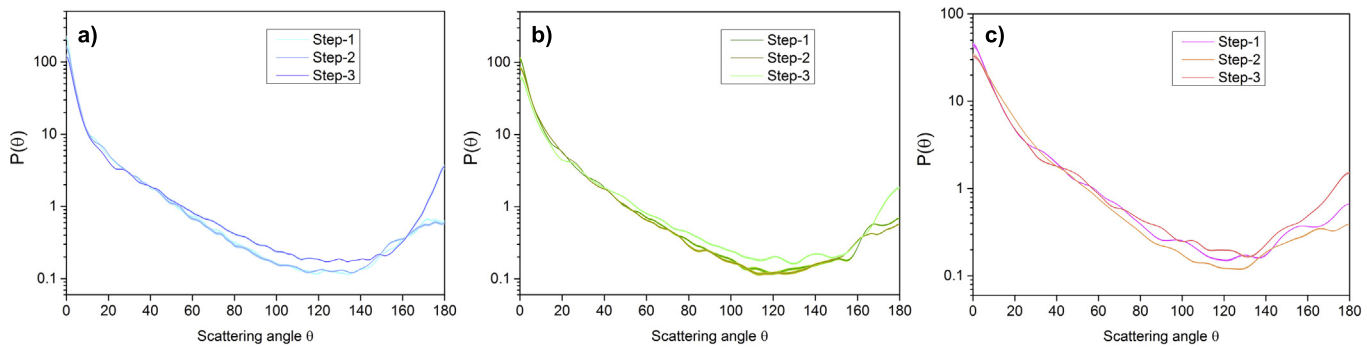


Fig. 10. Aerosol phase functions calculated for Step-1, Step-2 and Step-3 at: 355 nm (a), 532 nm (b) and 1064 nm (c).

0.22, 0.75 ± 0.16 and $0.31 \pm 0.08 \text{ Mm}^{-1} \text{ sr}^{-1}$, respectively. Final results were characterized by low RMSE ($0.36, 0.08$ and $0.04 \text{ Mm}^{-1} \text{ sr}^{-1}$) and a high linear correlation (R^2 of $0.992, 0.992$ and 0.994). Most importantly, in this case, slopes were close to one ($1.368, 0.931$ and 0.977 , respectively). Results also agreed with independent ground measurements of the scattering coefficient: $11.56 \pm 1.25 \text{ Mm}^{-1}$ from optical property calculations (at 532 nm) for $11.13 \pm 1.24 \text{ Mm}^{-1}$ determined at the same time by the nephelometer at 530 nm.

From the aforementioned results, this work highlights several important conclusions. First of all, the obtained data suggest that the presence in the atmosphere of aerosol components other than that routinely in PM samples (e.g. water-soluble, EC/OM) is fundamental in understanding the aerosol optical properties in the Arctic. In this respect, high latitude dust sources (e.g., Icelandic dust) play an important role; moreover, due to the expected reduction of the ice-covered surfaces in the Arctic, the impact of the high latitude dust sources on the Arctic aerosol optical properties is expected to grow in the future.

Thus, a complete and detailed determination of the aerosol composition is mandatory to finally predict the influence of aerosol on the Arctic climate. In this respect, this work underlines the importance of the integration of single particle and bulk chemical analysis for the characterization of optical properties in the Arctic.

Finally, the closure results were obtained in a case study belonging to a cluster of vertical profiles occurring for ~68% of the time over Ny-Ålesund. Thus, future closure investigations are called for in order to determine the role of other aerosol components under different vertical distribution (and transport) conditions.

Acknowledgements

This paper is an output of the GEMMA center in the framework of “Project MIUR – Dipartimenti di Eccellenza 2018–2022”.

This paper is also an output of the AMIS project in the framework of “Project MIUR – Dipartimenti di Eccellenza 2018–2022”.

The scientific activity in Ny Alesund was carried out in the framework of the CNR Polar Program. We thank the PRIN2009 “ARCTICA” project for financial support. We thank the Alfred-Wegener Institut for logistical support. We thank both Brent Holben and Piotr Sobolewski for their effort in establishing and maintaining the AERONET Hornsund site. Finally, we thank LSI-Lastem for the cooperation concerning meteorological instruments.

Appendix A. Supplementary data

Supplementary data to this article can be found online at <https://doi.org/10.1016/j.scitotenv.2019.05.399>.

References

- Ackerman, T.P., Toon, O.B., 1981. Absorption of visible radiation in atmosphere containing mixtures of absorbing and nonabsorbing particles. *Appl. Opt.* 20, 3661–3668, 1981.
- Ansmann, A., Riebesell, M., Wandinger, U., Weitkamp, C., Voss, E., Lahmann, W., Michaelis, W., 1992. Combined raman elastic-backscatter LIDAR for vertical profiling of moisture, aerosol extinction, backscatter, and LIDAR ratio. *Applied Physics B Photophysics and Laser Chemistry* 55, 18–28. <https://doi.org/10.1007/BF02246796>.
- Aspnes, D.E., 1982. Local-field effects and effective medium theory: a microscopic perspective. *Am. J. Phys.* 50, 704–709.
- Balkanski, Y., Schulz, M., Claiquin, T., Guibert, S., 2007. Reevaluation of mineral aerosol radiative forcings suggests a better agreement with satellite and AERONET data. *Atmos. Chem. Phys.* 7, 81–95. <https://doi.org/10.5194/acp-7-81-2007>.
- Ban-Weiss, G.A., Cao, L., Bala, G., Caldeira, K., 2011. Dependence of climate forcing and response on the altitude of black carbon aerosols. *Clim. Dyn.* 38 (5–6), 897–911. <https://doi.org/10.1007/s00382-011-1052-y>.
- Baron, P.A., Willeke, K., 2005. *Aerosol measurements. Principles, Techniques and Applications*, Second edition Wiley-Interscience.
- Barthelmy, D., 2006. Mineralogy Database. <http://www.webmineral.com>, Accessed date: 28 January 2019.
- Bates, T.S., Quinn, P.K., Johnson, J.E., Corless, a., Brechtel, F.J., Stalin, S.E., Meinig, C., Burkhardt, J.F., 2013. Measurements of atmospheric aerosol vertical distributions above Svalbard, Norway, using unmanned aerial systems (UAS). *Atmos. Meas. Tech.* 6 (8), 2115–2120. <https://doi.org/10.5194/amt-6-2115-2013>.
- Bindi, M., Brown, S., Camilloni, I., Diedhiou, A., Djalante, R., Ebi, K.L., et al., 2018. Chapter 3: impacts of 1.5°C global warming on natural and human systems. *Global Warming of 1.5°C IPCC Report 2018*, pp. 175–311. <https://www.ipcc.ch/sr15/>.
- Bohren, C.F., Huffman, D.R., 1983. *Absorption and Scattering of Light by Small Particles*. John Wiley, New York, NY.
- Bond, T.C., Bergstrom, R.W., 2006. Light absorption by carbonaceous particles: an investigative review. *Aerosol Sci. Technol.* 40, 27–67. <https://doi.org/10.1080/02786820500421521>.
- Brock, C.A., Cozic, J., Bahreini, R., Froyd, K.D., Middlebrook, A.M., McComiskey, A., Brioude, J., Cooper, O.R., Stohl, A., Aikin, K.C., de Gouw, J.A., Fahey, D.W., Ferrare, R.A., Gao, R.-S., Gore, W., Holloway, J.S., et al., 2011. Characteristics, sources, and transport of aerosols measured in spring 2008 during the aerosol, radiation, and cloud processes affecting Arctic Climate (ARCPAC) Project. *Atmos. Chem. Phys.* 11 (6), 2423–2453. <https://doi.org/10.5194/acp-11-2423-2011> (2011).
- Bruggeman, D., 1935. Calculation of various physics constants in heterogenous substances. I. Dielectricity constants and conductivity of mixed bodies from isotropic substances. *Ann. Phys.-Berlin* 24, 636–664.
- Cappelletti, D., Azzolini, R., Langone, L., Ventura, S., Viola, A., Aliani, S., et al., 2016. Environmental changes in the Arctic: an Italian perspective. *Rend. Lincei* 27, 1–6. <https://doi.org/10.1007/s12210-016-0555-1>.
- Chaijkovsky, A., Dubovik, O., Holben, B., Bril, A., Goloub, P., Tanré, D., Pappalardo, G., Wandinger, U., Chaijkowskaya, L., Denisov, S., Grudo, J., Lopatin, A., Karol, Y., Lapyonok, T., Amiridis, V., Ansmann, A., Apituley, A., Allados-Arboledas, L., Binietoglu, I., Boselli, A., D'Amico, G., Freudenthaler, V., Giles, D., Granados-Muñoz, M.J., Kokkalis, P., Nicolae, D., Oshchepkov, S., Papayannis, A., Rita Perrone, M., Pietruczuk, A., Rocadenbosch, F., Sicard, M., Slutsker, I., Talianu, C., De Tomasi, F., Tsekeri, A., Wagner, J., Wang, X., 2016. Lidar-Radiometer Inversion Code (LIRIC) for the retrieval of vertical aerosol properties from combined lidar/radiometer data: development and distribution in EARLINET. *Atmos. Meas. Tech.* 9, 1181–1205. <https://doi.org/10.5194/amt-9-1181-2016>.
- Chazette, P., Liousse, C., 2001. A case study of optical and chemical ground apportionment for urban aerosols in Thessa- loniki. *Atmos. Environ.* 35, 2497–2506. [https://doi.org/10.1016/S1352-2310\(00\)00425-8](https://doi.org/10.1016/S1352-2310(00)00425-8).
- Clegg, S.L., Brimblecombe, P., Wexler, A.S., 1998. Thermodynamic model of the system $\text{H}^+ \text{NH}_4^+ \text{SO}_4^- \text{NO}_3^- \text{H}_2\text{O}$ at tropospheric temperatures. *J. Phys. Chem. A* 102, 2137–2154.
- Crosbie, A.L., Davidson, G.W., 1985. Dirac-Delta approximations to the scattering phase function. *J. Quant. Spectrosc. Ra.* 33, 391–409.
- Dall’Osto, M., Beddows, D.C.S., Tunved, P., Krejci, R., Ström, J., Hansson, H.C., Yoon, Y.J., Park, K.T., Becagli, S., Udisti, R., et al., 2017. Arctic sea ice melt leads to atmospheric new particle formation. *Sci. REP-UK* 7, 3318. <https://doi.org/10.1038/s41598-017-03328-1>.
- Di Liberto, L., Angelini, F., Pietroni, I., Cairo, F., Di Donfrancesco, G., Viola, a., Argentini, S., Fierli, F., Gobbi, G., Maturilli, M., Neuber, R., Snels, M., 2012. Estimate of the Arctic convective boundary layer height from Lidar observations: a case study. *Adv. Meteorol.* 2012, 1–9. <https://doi.org/10.1155/2012/851927>.

- Eleftheriadis, K., Vratolis, S., Nyeki, S., 2009. Aerosol black carbon in the European Arctic: measurements at Zeppelin station, Ny-Ålesund, Svalbard from 1998–2007. *Geophys. Res. Lett.* 36 (2). <https://doi.org/10.1029/2008GL035741>.
- Engvall, A.-C., Krejci, R., Ström, J., Minikin, A., Trefeisen, R., Stohl, A., Herber, A., 2008. In-situ airborne observations of the microphysical properties of the Arctic tropospheric aerosol during late spring and summer. *Tellus B* <https://doi.org/10.1111/j.1600-0889.2008.00348.x> 080414161623888.
- Ferrero, L., Perrone, M.G., Petraccone, S., Sangiorgi, G., Ferrini, B.S., Lo Porto, C., Lazzati, Z., Cocchi, D., Bruno, F., Greco, F., Riccio, a., Bolzacchini, E., 2010. Vertically-resolved particle size distribution within and above the mixing layer over the Milan metropolitan area. *Atmos. Chem. Phys.* 10, 3915–3932. <https://doi.org/10.5194/acp-10-3915-2010>.
- Ferrero, L., Mocnik, G., Ferrini, B.S., Perrone, M.G., Sangiorgi, G., Bolzacchini, E., 2011a. Vertical profiles of aerosol absorption coefficient from micro-Aethalometer data and Mie calculation over Milan. *Sci. Total Environ.* 409 (14), 2824–2837. <https://doi.org/10.1016/j.scitotenv.2011.04.022>.
- Ferrero, L., Riccio, a., Perrone, M.G., Sangiorgi, G., Ferrini, B.S., Bolzacchini, E., 2011b. Mixing height determination by tethered balloon-based particle soundings and modeling simulations. *Atmos. Res.* 102 (1–2), 145–156. <https://doi.org/10.1016/j.atmosres.2011.06.016>.
- Ferrero, L., Cappelletti, D., Moroni, B., Sangiorgi, G., Perrone, M.G., Crocchianti, S., Bolzacchini, E., 2012. Wintertime aerosol dynamics and chemical composition across the mixing layer over basin valleys. *Atmos. Environ.* 56, 143–153. <https://doi.org/10.1016/j.atmosenv.2012.03.071>.
- Ferrero, L., Sangiorgi, G., Ferrini, B.S., Perrone, M.G., Moscatelli, M., D'Angelo, L., Rovelli, G., Ariatta, A., Truccolo, R., Bolzacchini, E., 2013. Aerosol corrosion prevention and energy-saving strategies in the design of green data centers. *Environ. Sci. Technol.* 47, 3856–3864. <https://doi.org/10.1021/es304790f> (2013).
- Ferrero, L., Castelli, M., Ferrini, B.S., Moscatelli, M., Perrone, M.G., Sangiorgi, G., Rovelli, G., D'Angelo, L., Moroni, B., Scardazza, F., Mocnik, G., Bolzacchini, E., Petitta, M., Cappelletti, D., 2014. Impact of Black Carbon Aerosol over Italian basin valleys: high resolution measurements along vertical profiles, radiative forcing and heating rate. *Atmos. Chem. Phys.* 14, 9641–9664.
- Ferrero, L., D'Angelo, L., Rovelli, G., Sangiorgi, G., Perrone, M.G., Moscatelli, M., Casati, M., Rozzoni, V., Bolzacchini, E., 2015. Determination of aerosol deliquescence and crystallization relative humidity for energy saving in free-cooled data centers. *Int. J. Environ. Sci. Technol.* 12 (9), 2777–2790. <https://doi.org/10.1007/s13762-014-0680-2>.
- Ferrero, L., Cappelletti, D., Busetto, M., Mazzola, M., Lupi, A., Lanconelli, C., Becagli, S., Traversi, R., Caiazzo, L., Giardi, F., et al., 2016. Vertical profiles of aerosol and black carbon in the Arctic: a seasonal phenomenology along 2 years (2011–2012) of field campaigns. *Atmos. Chem. Phys.* 16, 12601–12629. <https://doi.org/10.5194/acp-16-12601-2016>.
- Ferrero, L., Sangiorgi, G., Perrone, M.G., Rizzi, C., Cataldi, M., Markuszewski, P., Pakszys, P., Makuch, P., Petelski, T., Becagli, S., Traversi, R., Bolzacchini, E., Zielinski, T., 2019. Chemical composition of aerosol over the Arctic Ocean from summer ARctic EXPedition (AREX) 2011–2012 cruises: ions, amines, elemental carbon, organic matter, polycyclic aromatic hydrocarbons, n-alkanes, metals, and rare earth elements. *Atmosphere* 10 (54), 1–32. <https://doi.org/10.3390/atmos10020054>.
- Fierz, M., Houle, C., Steigemeier, P., Burtscher, H., 2011. Design, calibration, and field performance of a miniature diffusion size classifier. *Aerosol Sci. Technol.* 45 (1), 1–10. <https://doi.org/10.1080/02786826.2010.516283>.
- Fierz-Schmidhauser, R., Zieger, P., Gysel, M., Kammermann, L., DeCarlo, P.F., Baltensperger, U., Weingartner, E., 2010. Measured and predicted aerosol light scattering enhancement factors at the high alpine site Jungfraujoch. *Atmos. Chem. Phys.* 10, 2319–2333. <https://doi.org/10.5194/acp-10-2319-2010> (2010).
- Flanner, M.G., 2013. Arctic climate sensitivity to local black carbon. *J. Geophys. Res. Atmos.* 118 (4), 1840–1851. <https://doi.org/10.1002/jgrd.50176>.
- Francis, J.A., Hunter, E., 2006. New insight into the disappearing Arctic sea ice. *EOS Trans. Am. Geophys. Union* 87, 509–511, 2006.
- Freudenthaler, V., Esselborn, M., Wiegner, M., Heese, B., Tesche, M., Ansmann, A., Müller, D., Althausen, D., Wirth, M., Fix, A., Ehret, G., Knippertz, P., Toledano, C., Gasteiger, J., Garhammer, M., Seefeldner, M., 2009. Depolarization ratio profiling at several wavelengths in pure Saharan dust during SAMUM 2006. *Tellus Ser. B Chem. Phys. Meteorol.* 61, 165–179. <https://doi.org/10.1111/j.1600-0889.2008.00396.x>.
- Giardi, F., Becagli, S., Traversi, R., Frosini, D., Severi, M., Caiazzo, L., Ancillotti, C., Cappelletti, D., Moroni, B., Grotti, M., Bazzano, A., Lupi, A., Mazzola, M., Vitale, V., Malandrino, M., Ferrero, L., Bolzacchini, E., Viola, A., Udisti, R., 2016. Size distribution and ion composition of aerosol collected at Ny-Ålesund in the spring–summer field campaign 2013. *Rend. Lincei* 27, S47–S58. <https://doi.org/10.1007/s12210-016-0529-3>.
- Groot Zwaaftink, C.D., Grythe, H., Skov, H., Stohl, A., 2016. Substantial contribution of northern high-latitude sources to mineral dust in the Arctic. *J. Geophys. Res. Atmos.* 121 (13), 678–697. <https://doi.org/10.1002/2016JD025482>.
- Groot Zwaaftink, C.D., Arnalds, O., Dagsson-Waldhauserova, P., Eckhardt, S., Prospero, J.M., Stohl, A., 2017. Temporal and spatial variability of Icelandic dust emission and atmospheric transport. *Atmos. Chem. Phys.* 17 (1400), 10865–10878. <https://doi.org/10.5194/acp-17-10865-2017>.
- Guyon, P., Boucher, O., Graham, B., Beck, J., Mayol-Bracero, O.L., Roberts, G.C., Maenhaut, W., Artaxo, P., Andreae, M.O., 2003. Refractive index of aerosol particles over the Amazon tropical forest during LBA-EUSTACH 1999. *J. Aerosol Sci.* 34, 883–907. [https://doi.org/10.1016/S0021-8502\(03\)00052-1](https://doi.org/10.1016/S0021-8502(03)00052-1).
- Hansen, J., Nazarenko, L., 2004. Soot climate forcing via snow and ice albedo. *Proc. Natl. Acad. Sci.* 101, 423–428. www.pnas.org/doi/10.1073/pnas.2237157100.
- Heim, M., Mullins, B.J., Umhauer, H., Kasper, G., 2008. Performance evaluation of three optical particle counters with an efficient “multimodal” calibration method. *J. Aerosol Sci.* 39 (12), 1019–1031. <https://doi.org/10.1016/j.jaerosci.2008.07.006>.
- Heller, W., 1965. Remarks on refractive index mixture rules. *J. Phys. Chem.* 69, 1123–1129.
- Hess, M., Koepke, P., Schult, I., 1998. Optical properties of aerosols and clouds: the software package OPAC. *B. Am. Meteorol. Soc.* 79, 831–844. [https://doi.org/10.1175/1520-0477\(1998\)079<0831:OPOAAC>2.0.CO](https://doi.org/10.1175/1520-0477(1998)079<0831:OPOAAC>2.0.CO).
- Heyder, J., Gebhart, J., 1979. Optimization of response functions of light scattering instruments for size evaluation of aerosol particles. *Appl. Opt.* 18 (5), 705–711.
- Hoffmann, A., 2012. Comparative Aerosol Study Based on Multi-wavelength RAMAN Lidar at Ny Ålesund, Spitzbergen. Ph. D Thesis (Potsdam). http://epic.awi.de/25751/1/Hoffmann_aerosolclosure2012.pdf.
- Hoffmann, A., Ritter, C., Stock, M., Shiobara, M., Lampert, A., Maturilli, M., Orgis, T., Neuber, R., 2009. Ground-based lidar measurements from Ny-Ålesund during ASTAR. *Atmos. Chem. Phys.* 9, 9059–9081 2009 www.atmos-chem-phys.net/9/9059/2009/.
- Hoffmann, A., Osterloh, L., Stone, R., Lampert, A., Ritter, C., Stock, M., Tunved, P., Hennig, T., Böckmann, C., Li, S.-M., Eleftheriadis, K., Maturilli, M., Orgis, T., Herber, A., Neuber, R., Dethloff, K., 2012. Remote sensing and in-situ measurements of tropospheric aerosol, a PAMARCMiP case study. *Atmos. Environ.* 52, 56–66. <https://doi.org/10.1016/j.atmosenv.2011.11.027>.
- Howell, S.G., Clarke, A.D., Shinozuka, Y., Kapustin, V., McNaughton, C.S., Huebert, B.J., 2006. Influence of relative humidity upon pollution and dust during ACE-Asia: size distributions and implications for optical properties. *J. Geophys. Res.* 111, D06205. <https://doi.org/10.1029/2004JD005759>.
- Hueglin, C., Gehrig, R., Baltensperger, U., Gysel, M., Monn, C., Vonmont, H., 2005. Chemical characterisation of PM2.5, PM10 and coarse particles at urban, near-city and rural sites in Switzerland. *Atmos. Environ.* 39, 637–651. <https://doi.org/10.1016/j.atmosenv.2004.10.027>.
- Intrieri, J.M., Fairall, C.W., Shupe, M.D., Persson, P.O.G., Andreas, E.L., Guest, P.S., Moritz, R.E., 2002. Annual cycle of Arctic surface cloud forcing at SHEBA. *J. Geophys. Res.* 107 (C10). <https://doi.org/10.1029/2000JC000439>.
- IPCC, 2013. Climate Change 2013: The Physical Science Basis. Cambridge University Press, Cambridge, United Kingdom and New York, USA (2013).
- Jacob, D.J., Crawford, J.H., Maring, H., Clarke, A.D., Dibb, J.E., Emmons, L.K., Ferrare, R.A., Hostetter, C.A., Russell, P.B., Singh, H.B., Thompson, A.M., Shaw, G.E., McCauley, E., Pederson, J.R., Fisher, J.A., 2010. The Arctic Research of the Composition of the Troposphere from Aircraft and Satellites (ARCTAS) mission: design, execution, and first results. *Atmos. Chem. Phys.* 10, 5191–5212. <https://doi.org/10.5194/acp-10-5191-2010>.
- Kandler, K., Benker, N., Bunde, U., Cuevas, E., Ebert, M., Knippertz, P., Rodríguez, S., Schütz, L., Weinbruch, S., 2007. Chemical composition and complex refractive index of Saharan Mineral Dust at Izaña, Tenerife (Spain) derived by electron microscopy. *Atmos. Environ.* 41, 8058–8074. <https://doi.org/10.1016/j.atmosenv.2007.06.047>.
- Kaufman, Y.J., Tanré, D., Boucher, O., 2002. A satellite view of aerosols in the climate system. *Nature* 419, 215–223.
- Koch, D., Schulz, M., Kinne, S., McNaughton, C., Spackman, J.R., Balkanski, Y., Bauer, S., Berntsen, T., Bond, T.C., Boucher, O., Chin, M., Clarke, A., De Luca, N., Dentener, F., Diehl, T., Dubovik, O., Easter, R., Fahey, D.W., Feichter, J., Fillmore, D., Freitag, S., Ghan, S., Ginoux, P., Gong, S., Horowitz, L., Iversen, T., Kirkevåg, A., Klimont, Z., Kondo, Y., Krol, M., Liu, X., Miller, R., Montanaro, V., Moteki, N., Myhre, G., Penner, J.E., Perlitz, J., Pitari, G., Reddy, S., Sahu, L., Sakamoto, H., Schuster, G., Schwarz, J.P., Seland, Ø., Stier, P., Takegawa, N., Takemura, T., Textor, C., van Aardenne, J.A., Zhao, Y., 2009. Evaluation of black carbon estimations in global aerosol models. *Atmos. Chem. Phys.* 9, 9001–9026. <https://doi.org/10.5194/acp-9-9001-2009>.
- Koren, I., Kaufman, Y.J., Remer, L.A., Martins, J.V., 2004. Measurements of the effect of amazon smoke on inhibition of cloud formation. *Science* 303, 1342–1345.
- Koren, I., Martins, J.V., Remer, L.A., Afargan, H., 2008. Smoke invigoration versus inhibition of clouds over the amazon. *Science* 321, 946–949.
- Kupiszewski, P., Leck, C., Tjernström, M., Sjögren, S., Sedlar, J., Graus, M., Müller, M., Brooks, B., Swietlicki, E., Norris, S., Hansel, A., 2013. Vertical profiling of aerosol particles and trace gases over the central Arctic Ocean during summer. *Atmos. Chem. Phys.* 13 (24), 12405–12431. <https://doi.org/10.5194/acp-13-12405-2013>.
- Lesins, G., Chylek, P., Lohmann, U., 2002. A study of internal and external mixing scenarios and its effect on aerosol optical properties and direct radiative forcing. *J. Geophys. Res.* 107, AAC5.1–AAC5.12. <https://doi.org/10.1029/2001JD000973>.
- Liu, Y., Daum, P.H., 2008. Relationship of refractive index to mass density and self-consistency of mixing rules for multicomponent mixtures like ambient aerosols. *J. Aerosol Sci.* 39, 974–986. <https://doi.org/10.1016/j.jaerosci.2008.06.006>.
- Ma, X., Lu, J.Q., Brock, R.S., Jacobs, K.M., Yang, P., Hu, X.-H., 2003. Determination of complex refractive index of polystyrene microspheres from 370 to 1610 nm. *Phys. Med. Biol.* 48, 4165–4172.
- Maturilli, M., Kayser, M., 2016. Arctic warming, moisture increase and circulation changes observed in the Ny-Ålesund homogenized radiosonde record. *Theor. Appl. Climatol.*, 1–17 <https://doi.org/10.1007/s00704-016-1864-0>.
- Markowicz, K.M., Ritter, C., Lisok, J., Makuch, P., Stachelska, I.S., Cappelletti, D., Mazzola, M., Chilinski, M.T., 2017. Vertical variability of aerosol single-scattering albedo and equivalent black carbon concentration based on in-situ and remote sensing techniques during the iAREA campaigns in Ny-Ålesund. *Atmos. Environ.* 164, 431–447. <https://doi.org/10.1016/j.atmosenv.2017.06.014>.
- Mazzola, M., Busetto, M., Ferrero, L., Viola, A., Pietro, C., Cappelletti, D., 2016. AGAP: an atmospheric gondola for aerosol profiling. *Rendiconti Lincei* 27, 105–113. <https://doi.org/10.1007/s12210-016-0514-x>.
- Mishchenko, M.I., Travis, L.D., Kahn, R.A., West, R.A., 1997. Modeling phase functions for dustlike tropospheric aerosols using a shape mixture of randomly oriented polydisperse spheroids. *J. Geophys. Res.* 102, 16 831–16 847.
- Moroni, B., Becagli, S., Bolzacchini, E., Busetto, M., Cappelletti, D., Crocchianti, S., Ferrero, L., Frosini, D., Lanconelli, C., Lupi, A., Maturilli, M., Mazzola, M., Perrone, G., Sangiorgi, G., Traversi, R., Udisti, R., Viola, A., Vitale, V., 2015. Vertical profiles and chemical properties of aerosol particles upon Ny-Ålesund (Svalbard Islands). *Ad. Meteorol.* 2015 (292081), 1–11.

- Moroni, B., Cappelletti, D., Ferrero, L., Crocchianti, S., Busetto, M., Mazzola, M., Becagli, S., Traversi, R., Udisti, R., 2016. Local vs. long-range sources of aerosol particles upon Ny-Ålesund (Svalbard Islands): mineral chemistry and geochemical records. *Rendiconti Lincei* 27, 115–127. <https://doi.org/10.1007/s12210-016-0533-7>.
- Moroni, B., Arnalds, O., Dagsson-Waldhauserová, P., Crocchianti, S., Vivani, R., Cappelletti, D., 2018. Mineralogical and chemical records of Icelandic dust sources upon Ny-Ålesund (Svalbard Islands). *Front. Earth Sci.* 6. <https://doi.org/10.3389/feart.2018.00187>.
- Navarro, J.C.A., Varma, V., Riipinen, I., Seland, Kirkevåg, A., Struthers, H., Iversen, T., Hansson, H.C., Ekman, A.M.L., 2016. Amplification of Arctic warming by past air pollution reductions in Europe. *Nat. Geosci.* 9, 277–281. <https://doi.org/10.1038/ngeo2673>.
- Pathak, R., 2004. Characteristics of aerosol acidity in Hong Kong. *Atmos. Environ.* 38, 2965–2974. <https://doi.org/10.1016/j.atmosenv.2004.02.044>.
- Pesava, P., Horvath, H., Kasahara, M., 2001. A local optical closure experiment in Vienna. *J. Aerosol Sci.* 32, 1249–1267. [https://doi.org/10.1016/S0021-8502\(01\)00053-2](https://doi.org/10.1016/S0021-8502(01)00053-2).
- Quinn, P.K., Bates, T.S., Baum, E., Doubleday, N., Fiore, A.M., Flanner, M., Fridlind, A., Garrett, T.J., Koch, D., Menon, S., Shindell, D., Stohl, A., Warren, S.G., 2008. Short-lived pollutants in the Arctic: their climate impact and possible mitigation strategies. *Atmos. Chem. Phys.* 8, 1723–1735. <https://doi.org/10.5194/acp-8-1723-2008>.
- Ramanathan, V., Feng, Y., 2009. Air pollution, greenhouse gases and climate change: global and regional perspectives. *Atmos. Environ.* 43 (1), 37–50. <https://doi.org/10.1016/j.atmosenv.2008.09.063>.
- Randriamariisoa, H., Chazette, P., Couvert, P., Sanak, J., 2006. Relative humidity impact on aerosol parameters in a Paris suburban area. *Atmos. Chem. Phys.* 6, 1389–1407. <https://doi.org/10.5194/acp-6-1389-2006>.
- Samset, B.H., Myhre, G., Schulz, M., Balkanski, Y., Bauer, S., Berntsen, T.K., Bian, H., Bellouin, N., Diehl, T., Easter, R.C., Ghan, S.J., Iversen, T., Kinne, S., Kirkevåg, a., Lamarque, J.-F., Lin, G., Liu, X., Penner, J.E., Seland, Ø., Skeie, R.B., Stier, P., Takemura, T., Tsigaridis, K., Zhang, K., 2013. Black carbon vertical profiles strongly affect its radiative forcing uncertainty. *Atmos. Chem. Phys.* 13 (5), 2423–2434. <https://doi.org/10.5194/acp-13-2423-2013>.
- Sand, M., Berntsen, T.K., Kay, J.E., Lamarque, J.F., Seland, Ø., Kirkevåg, A., 2013. The Arctic response to remote and local forcing of black carbon. *Atmos. Chem. Phys.* 13 (1), 211–224. <https://doi.org/10.5194/acp-13-211-2013>.
- Sand, M., Berntsen, T.K., Von Salzen, K., Flanner, M.G., Lagner, J., Victor, D.G., 2015. Response of Arctic temperature to changes in emissions of short-lived climate forcers. *Nat. Clim. Chang.* 6, 286–290. <https://doi.org/10.1038/NCLIMATE2880>.
- Sangiorgi, G., Ferrero, L., Perrone, M.G., Bolzacchini, E., Duane, M., Larsen, B.R., 2011. Vertical distribution of hydrocarbons in the low troposphere below and above the mixing height: tethered balloon measurements in Milan, Italy. *Environ. Pollut.* 159 (12), 3545–3552. <https://doi.org/10.1016/j.envpol.2011.08.012>.
- Schumann, T., 1990. On the use of modified clean-room optical particle counter for atmospheric aerosols at high relative humidity. *Atmos. Res.* 25, 499–520. [https://doi.org/10.1016/0169-8095\(90\)90035-B](https://doi.org/10.1016/0169-8095(90)90035-B).
- Schuster, G.L., Dubovik, O., Holben, B.N., Clothiaux, E.E., 2005. Inferring black carbon content and specific absorption from Aerosol Robotic Network (AERONET) aerosol retrievals. *J. Geophys. Res.* 110. <https://doi.org/10.1029/2004JD004548> D10S17.
- Schwarz, J.P., Spackman, J.R., Gao, R.S., Watts, L.A., Stier, P., Schulz, M., Davis, S.M., Wofsy, S.C., Fahey, D.W., 2010. Global-scale black carbon profiles observed in the remote atmosphere and compared to models. *Geophys. Res. Lett.* 37 (18). <https://doi.org/10.1029/2010GL044372>.
- Screen, J.A., Simmonds, I., 2010a. The central role of diminishing sea ice in recent Arctic temperature amplification. *Nature* 464, 1334–1337.
- Screen, J.A., Simmonds, I., 2010b. Increasing fall-winter energy loss from the Arctic Ocean and its role in Arctic temperature amplification. *Geophys. Res. Lett.* 37, L16707. <https://doi.org/10.1029/2010GL044136>.
- Seinfeld, J.H., Pandis, S.N., 2006. *Atmos. Chem. Phys. – From Air Pollution to Climate Change*. Wiley-Interscience edition.
- Serreze, M.C., Barry, R.G., 2011. Processes and impacts of Arctic amplification: a research synthesis. *Glob. Planet. Change* 77 (1–2), 85–96. <https://doi.org/10.1016/j.gloplacha.2011.03.004>.
- Shindell, D., Faluvegi, G., 2009. Climate response to regional radiative forcing during the twentieth century. *Nat. Geosci.* 2 (4), 294–300. <https://doi.org/10.1038/ngeo473>.
- Spackman, J.R., Gao, R.S., Neff, W.D., Schwarz, J.P., Watts, L.A., Fahey, D.W., Holloway, J.S., Ryerson, T.B., Peischl, J., Brock, C.A., 2010. Aircraft observations of enhancement and depletion of black carbon mass in the springtime Arctic. *Atmos. Chem. Phys.* 10 (19), 9667–9680. <https://doi.org/10.5194/acp-10-9667-2010>.
- Stier, P., Seinfeld, J.H., Kinne, S., Boucher, O., 2007. Aerosol absorption and radiative forcing. *Atmos. Chem. Phys.* 7, 5237–5261. <https://doi.org/10.5194/acp-7-5237-2007>.
- Tesche, M., Zieger, P., Rastak, N., Charlson, R.J., Glantz, P., Tunved, P., Hansson, H.C., 2014. Reconciling aerosol light extinction measurements from spaceborne lidar observations and in situ measurements in the Arctic. *Atmos. Chem. Phys.* 14, 7869–7882. <https://doi.org/10.5194/acp-14-7869-2014>.
- Tunved, P., Ström, J., Krejci, R., 2013. Arctic aerosol life cycle: linking aerosol size distributions observed between 2000 and 2010 with air mass transport and precipitation at Zeppelin station, Ny-Ålesund, Svalbard. *Atmos. Chem. Phys.* 13 (7), 3643–3660. <https://doi.org/10.5194/acp-13-3643-2013>.
- Turpin, B.J., Lim, H.-J., 2001. Species contributions to PM2.5 mass concentrations: revisiting common assumptions for estimating organic mass. *Aerosol Sci. Technol.* 35, 602–610. <https://doi.org/10.1080/02786820119445>.
- Udisti, R., Becagli, S., Frosini, D., Ghedini, C., Rugi, F., Severi, M., Traversi, R., Zanini, R., Calzolai, G., Chiari, M., Lucarelli, F., Nava, S., Ardini, F., Grotti, M., Vione, D., Malandrino, M., Bolzacchini, E., Ferrero, L., Perrone, M.G., Sangiorgi, G., Francesconi, S., Giannarelli, S., Cappelletti, D., Moroni, B., Ceccato, D., Mittner, P., Sartori, P., 2013. *Activity and Preliminary Results From the 2011–2012 Field Seasons at Ny-Ålesund*. vol. DTA 14/2013. 2239-5172CNR Edizioni, pp. 53–68.
- Udisti, R., Bazzano, A., Becagli, S., Bolzacchini, E., Caiazzo, L., Cappelletti, D., Ferrero, L., Frosini, D., Giardi, F., Grotti, M., Lupi, A., Malandrino, M., Mazzola, M., Moroni, B., Severi, M., Traversi, R., Viola, A., Vitale, V., 2016. Sulfate source apportionment in the Ny Ålesund (Svalbard Islands) Arctic aerosol. *Rend. Fis. Acc. Lincei* 27 (1), S85–S94.
- Vavrus, S., Waliser, D., Schweiger, A., Francis, J.A., 2009. Simulations of 20th and 21st century Arctic cloud amount in the global climate models assessed in the IPCC AR4. *Climatic Dyn* 33, 1099–1115. <https://doi.org/10.1007/s00382-008-0475-6>.
- Vihma, T., Kilpeläinen, T., Manninen, M., Sjöblom, A., Jakobson, E., Palo, T., Jaagus, J., Maturilli, M., 2011. Characteristics of temperature and humidity inversions and low-level jets over Svalbard fjords in spring. *Adv. Meteorol.* 2011, 1–14. <https://doi.org/10.1155/2011/486807>.
- Yang, X.-Y., Fyfe, J.C., Flato, G.M., 2010. The role of poleward energy transport in Arctic temperature evolution. *Geophys. Res. Lett.* 37, L14803. <https://doi.org/10.1029/2010GL042487>.
- Zhang, Y., Seigneur, C., Seinfeld, J.H., Jacobson, M., Clegg, S.L., Binkowski, F.S., 2000. A comparative review of inorganic aerosol thermodynamic equilibrium modules: similarities, differences, and their likely causes. *Atmos. Environ.* 34, 117–137.